Quantifying HONO Production from Nitrate Photolysis in a Polluted Atmosphere

Yifan Jiang[1]*, Men Xia[1,2,3]*, Likun Xue[4], Xinfeng Wang[4], Xuelian Zhong[4], Yongchun Liu[3], Markku Kulmala[2,3], Tong Ma[5], Jiaqi Wang[5], Yurun Wang[1], Jian Gao[5], and Tao Wang[1]

[1]Department of Civil and Environmental Engineering, The Hong Kong Polytechnic University, Hong Kong, 999077, China

[2]Institute for Atmospheric and Earth System Research/Physics, Faculty of Science, University of Helsinki, Helsinki, 00014, Finland

[3]Aerosol and Haze Laboratory, Advanced Innovation Center for Soft Matter Science and Engineering, Beijing University of Chemical Technology, 100029, Beijing, China

[4]Environment Research Institute, Shandong University, Qingdao, 266237, China

[5]State Key Laboratory of Environmental Criteria and Risk Assessment, Chinese Research Academy of Environmental Sciences, Beijing, 100012, China

Correspondence to: Tao Wang (tao.wang@polyu.edu.hk) and Jian Gao (gaojian@craes.org.cn)

*These authors contributed equally to this work.

Abstract

The photolysis of particulate nitrate (pNO_3^-) has been suggested to be an important source of nitrous acid (HONO) in the troposphere. However, determining the photolysis rate constant of pNO_3^- ($j_{pNO_3^-}$) suffers from high uncertainty. Prior laboratory measurements of $j_{pNO_3^-}$ using aerosol filters have been complicated by the "shadow effect"—a phenomenon of light extinction within aerosol layers that potentially skews these measurements. We developed a method to correct the shadow effect on the photolysis rate constant of pNO_3^- for HONO production ($j_{pNO_3^-\rightarrow HONO}$) using aerosol filters with identical chemical compositions but different aerosol loadings. We applied the method to quantify $j_{pNO_3^-\rightarrow HONO}$ over the North China Plain (NCP) during the winter haze period. After correcting for the shadow effect, the normalized average $j_{pNO_3^-\rightarrow HONO}$ at 5 °C increased from 5.89×10^{-6} s^{-1} to 1.72×10^{-5} s^{-1}. The $j_{pNO_3^-\rightarrow HONO}$ decreased with increasing pH and nitrate proportions in $PM_{2.5}$ ($R_{NO_3^-}$) and had no correlation with nitrate concentrations. A parameterization for $j_{pNO_3^-\rightarrow HONO}$ was developed for model simulation of HONO production in NCP and similar environments.

Keywords

HONO production mechanisms, shadow effect, nitrate photolysis, winter haze, air quality

Table of Content art

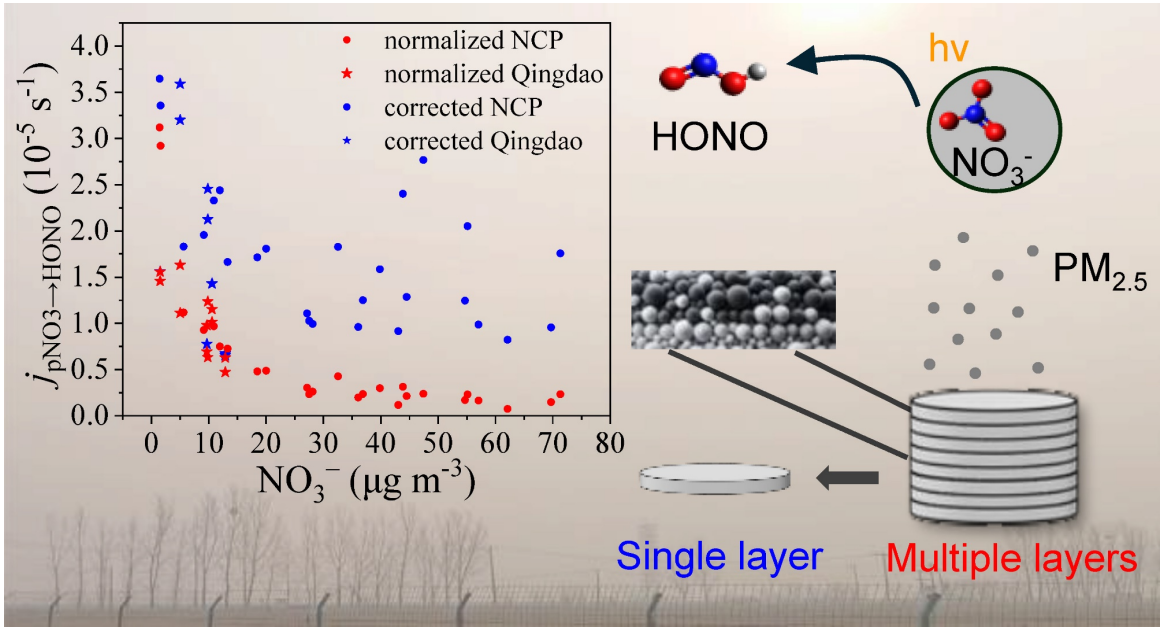

Synopsis

Previously measured $j_{pNO_3^-}$ values using the filter-based method suffer from high uncertainty due to the "shadow effect". Our research quantified this effect and improved the prediction of HONO production.

1. Introduction

Nitrous acid (HONO) plays a key role in tropospheric photochemistry, as it is a primary source of the hydroxyl radical (OH) during the daytime.[1–3] The contribution of HONO to OH production is generally more pronounced in polluted areas (e.g., 87% at an urban site[4]) than unpolluted areas (e.g., 33% in a forest[5]). A growing body of research has demonstrated significant enhancement of ozone and secondary aerosols by HONO, especially in polluted regions.[6,7] Sources of HONO include direct emissions, such as soil[8], vehicle exhausts[9], and biomass burning[10], as well as secondary formation, such as the gas-phase reaction between nitric oxide (NO) and OH[11], heterogeneous reactions of nitrogen

dioxide (NO_2) on ground and aerosol surfaces[12], and photolysis of particulate nitrate[13].

The photolysis of aqueous nitrate under actinic radiation ($\lambda > 290$ nm) proceeds through two main channels: the generation of NO_2 and OH (see R1) and the production of nitrite (NO_2^-) alongside $O(^3P)$ (see R2). HONO is subsequently formed through the protonation of NO_2^- (see R3).[14] The $j_{pNO_3^-}$ considers the production of both NO_2 and HONO, whereas $j_{pNO_3^- \to HONO}$ quantifies only HONO production. Recent findings suggest that the photolysis rate constant of pNO_3^- is considerably higher than that of bulk aqueous nitrate or gaseous nitric acid (HNO_3),[13,15–17] highlighting nitrate photolysis as a potentially substantial contributor to daytime HONO. However, accurately quantifying $j_{pNO_3^-}$ remains challenging, primarily because of the difficulty in precisely replicating the physical and chemical properties of atmospheric particles in the laboratory.

$$NO_3^- + h\nu\,(+H^+) \rightarrow NO_2 + \cdot OH \quad \text{(R1)}$$

$$NO_3^- + h\nu \rightarrow NO_2^- + O(^3P) \quad \text{(R2)}$$

$$NO_2^- + H^+ \leftrightarrow HONO(aq) \rightarrow HONO(g) \quad \text{(R3)}$$

The prevailing approach to measuring $j_{pNO_3^-}$ involves laboratory experiments in which ambient particles collected on filters are exposed to illumination.[13,15,16,18] This method calculates $j_{pNO_3^-}$ by dividing the NO_2 and HONO production rate by the total amount of nitrate on the filter. The primary uncertainties of this method arise from the distinct physical states of particles: those collected on filters are aggregated, in contrast to those suspended in ambient air. To address the deficiency, a recent study used suspended aerosols generated from pure nitrate salt solutions using an atomizer and calculated a much smaller $j_{pNO_3^-}$.[19] However, the applicability of this method is limited by the simplicity of the nitrate particle types used, which may not capture the complexity of ambient aerosols.

In addition to direct measurements of $j_{pNO_3^-}$, estimations of these values have been made through evaluating the budget of reactive nitrogen species by integrating modeling and field observations.[15,20–22] The $j_{pNO_3^-}$ values were derived after assuming that the missing source or sink of reactive nitrogen species stemmed solely from the photolysis of pNO_3^-, with HONO being the main product. Such calculated $j_{pNO_3^-}$ values are intrinsically affected by these assumptions, as well as by the uncertainties in quantifying other HONO sources (e.g., the heterogeneous uptake of NO_2 by various surfaces). Consequently, these derived values have been taken to represent the upper limit, and most estimations have been conducted in clean marine air, where the contributions of NO_2-related sources are negligible.

Previous filter-based methods have revealed a decreasing trend in $j_{pNO_3^-}$ with increasing nitrate loadings.[13,16,18,21] Ye et al. and Bao et al. attributed this to an intrinsic drawback of using ambient aerosol filters, termed the “shadow effect,” wherein particles

in the lower layers of aerosol filters receive less light because of the presence of particles in the upper layers.[13,16] However, a recent study[17] attributed this pattern to the "nitrate distribution effect," wherein HONO production is driven by the photolysis of surface-adsorbed nitrate rather than bulk nitrate[23,24]. In reality, the filter artifact and the nitrate distribution effect may both contribute to the observed decrease.

This study aimed to verify and quantify the shadow effect in the filter-based methods to derive true $j_{\mathrm{pNO_3^-\rightarrow HONO}}$ values in polluted atmosphere. We measured $j_{\mathrm{pNO_3^-\rightarrow HONO}}$ in a dynamic chamber using $PM_{2.5}$ samples collected from seven cities in northern China during winter haze. To quantify the shadow effect, two sets of filters were simultaneously collected to obtain the same aerosol chemical compositions but discrepant $PM_{2.5}$ loadings. A parameterization of corrected $j_{\mathrm{pNO_3^-\rightarrow HONO}}$ was developed, incorporating pH, nitrate proportions in $PM_{2.5}$ ($R_{\mathrm{NO_3^-}}$), and temperature.

2. Materials and Methods

2.1. Aerosol filter sampling across the North China Plain

Ambient $PM_{2.5}$ samples were collected on quartz filters in seven cities in northern China during the winter of 2017 and 2018, as described in Table 1. These cities are part of the "2+26" city clusters[25] in North China Plain (NCP) which experiences severe air pollution in winter due to unfavorable meteorological conditions and intensive anthropogenic emissions[26,27]. To eliminate organic artifacts, the quartz filters underwent a pre-firing process at a temperature of 900 ℃ for 4 hours. Following pre-firing, the filters were stored in a freezer at −20 ℃. Filter samples, each with a diameter of 47 mm, were obtained using the TH-16A air particulate intelligent sampler, which features four channels and operates at a flow rate of 16.67 Lpm. Sampling took place from 10:00 am local time (LT) until 09:00 am LT the following day. Water-soluble ions, including Na^+, NH_4^+, K^+, Mg^{2+}, Ca^{2+}, Cl^-, NO_3^-, and SO_4^{2-}, were extracted with Milli-Q water and measured by ion chromatography (Table S1). Further information regarding the instruments utilized can be found in previous papers.[28,29]

2.2. Aerosol filter sampling for the shadow effect experiment

Figure 1a illustrates the sampling settings employed in the experiment to quantify the shadow effect. We designed a procedure to collect aerosol filters with the same chemical compositions but different aerosol loadings using two samplers working simultaneously. These two samplers were set to different sampling rates to achieve varying thicknesses of collected particle layers in the parallel samplings. On the left-hand side of sets A and B, a

high-volume sampler (Tisch Environmental, TE-6070VXZ-2.5-HVS) operating at a flow rate of 1130 Lpm sampled aerosols on 20.3 cm × 25.4 cm quartz filters. On the right-hand side, a medium-volume sampler (TH-150D II), with a flow rate of 100 Lpm for set A and 50 Lpm for set B, sampled aerosols on filters, each with a diameter of 150 mm. In each set, we sampled for 3 h, 6 h, and 18 h to get three sets of aerosol loadings. To ensure consistency in the aerosol chemical compositions, the sampling periods were the same for each pair of parallel samplings, as denoted by the shared colors in Figure 1a. The filters were collected during the winter of 2022 atop a five-story office building in the Entrepreneurship Center of Blue Silicon Valley located in a rural site in Qingdao, a coastal city in northern China (36.35° N, 120.67° E). Detailed sampling information is provided in Table 2.

2.3. Aerosol photochemical aging experiments

The experimental setup is depicted in Figure 1c. The photochemical experiments were conducted in a dynamic chamber 25 cm in length, 15 cm in width, and 4 cm in height with a transparent Teflon window at the top. Part of the filter was cut and placed in a quartz petri dish (inner diameter: 35 mm; inner height: 7 mm) located at the center of the chamber. A high-pressure xenon lamp was used to mimic sunlight, and its spectral irradiance is shown in Figure 1b. The xenon lamp had a smaller photon flux in the 300–326 nm range than that of the standard air mass 1.5 solar irradiation (AM1.5), which corresponds to a solar zenith angle of 48.2°. However, the xenon lamp exhibited a larger photon flux in the 326–420 nm range. The reaction products were delivered to the chamber's outflow using zero air produced by a zero-air generator (Environics, model 7000) as the carrier gas. To replicate winter conditions in the NCP, the temperature of the reactor was maintained at 5 ℃ using an ice bath in a cooler box. Additionally, the relative humidity (RH) in the chamber was adjusted to 50%. Before introducing filter samples into the chamber, the background HONO concentration was measured while a continuous flow of zero air and illumination was applied for 10 minutes. After ensuring at least 1 h of irradiation, 40 ppb of O_3, which represents a relatively high level of O_3 during winter in the NCP, was added to the chamber using a dynamic calibrator. Then, the targeted O_3 concentration was monitored and confirmed using an O_3 analyzer connected to the outflow of the chamber (Thermo Scientific Model 49i). The xenon lamp was equipped with an AM1.5 filter (which filters out light with a wavelength below 360 nm) and a 300–800 nm filter (which allows light with a wavelength in the range of 300–800 nm to pass through) to investigate the wavelength dependency of pNO_3^- photolysis.

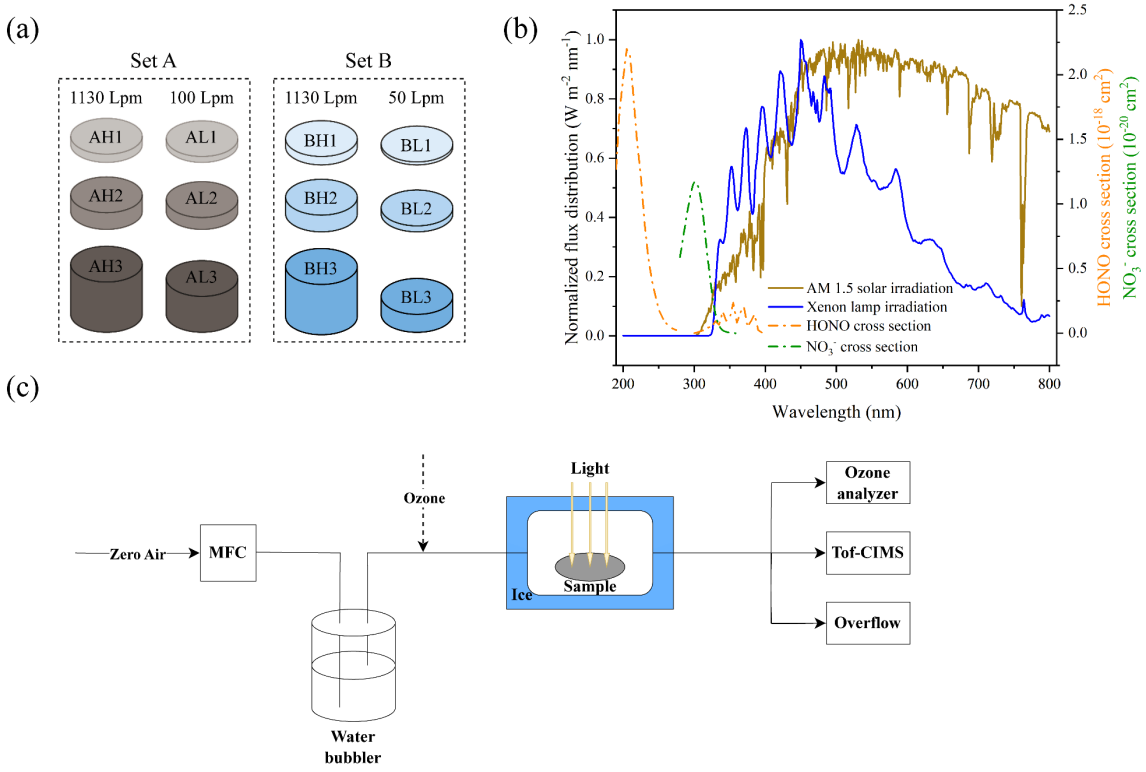

Figure 1. Setup of dynamic chamber experiments. (a) Sampling settings of the shadow effect experiment. AH denotes the sample obtained at a higher flow rate (1130 Lpm) and AL indicates a lower flow rate (100 Lpm). The labels "BH" and "BL" follow a similar nomenclature. (b) Irradiation spectrum of the xenon lamp used in this study and the absorption cross-sections of HONO (IUPAC; http://iupac.pole-ether.fr/index.html) and aqueous nitrate[30]. (c) Schematic diagram of the photochemical aging experimental setup. MFC represents mass flow controller.

The average production rate of HONO (P_{HONO}, mol s^{-1}) during irradiation was calculated via the following equation (eq. 1)[16]:

$$P_{HONO} = \left(\frac{F}{V_m \times t} + j_{HONO} \times \frac{V}{V_m \times t}\right) \times 10^{-9} \times \int_0^t (C_{HONO} - C_{HONO-bkg})\,dt \quad (1)$$

where F is the flow rate of the carrier gas (L min^{-1}); j_{HONO} (0.00517 s^{-1}) is the photolysis rate constant of HONO under the irradiation of the xenon lamp at a 15-cm height (see Text S1); V is the volume of the reactor chamber (L); V_m (22.8 L mol^{-1}) is the molar volume of gas at 5 °C and 1 atm; t is the duration of the irradiation, for which we used 15 min for consistency with previous studies[13,16]; and C_{HONO} and $C_{HONO\text{-}bkg}$ (ppb) are the mixing ratios of HONO in the chamber after and before adding the sample.

$j_{pNO_3^- \rightarrow HONO}$ was calculated by dividing P_{HONO} by the total nitrate in the $PM_{2.5}$ samples and further normalized to tropical noontime conditions on the ground (solar zenith

angle $\theta = 0°$), where the photolysis rate constant of aqueous nitrate is 3.23×10^{-5} s^{-1} with quantum yield equal to 1 (eq. 2), as calculated using the tropospheric ultraviolet and visible radiation model.

$$j_{pNO_3^- \rightarrow HONO} = \frac{P_{HONO}}{n_{NO_3^-}} \times \frac{3.23 \times 10^{-5}}{j_{exp}} \quad (2)$$

where $n_{NO_3^-}$ (mol) is the amount of nitrate in the $PM_{2.5}$ sample; and j_{exp} (s^{-1}) is the photolysis rate constant of aqueous nitrate, with quantum yield equal to 1, under xenon lamp irradiation. Here, j_{exp} was calculated as 8.85×10^{-6} s^{-1} (Text S1).

To quantify the shadow effect, we introduced the parameter "light efficiency" (*LE*), which describes the efficiency of light's penetration of the particles (eq. 3).

$$LE = \frac{P_{HONO-H}/P_{HONO-L}}{n_{NO_3^--H}/n_{NO_3^--L}} \times 100\% = \frac{j_{pNO_3^- \rightarrow HONO-H}}{j_{pNO_3^- \rightarrow HONO-L}} \times 100\% \quad (3)$$

where the suffixes H and L represent filters with higher loadings and lower loadings of particles in each pair of comparative experiments, respectively.

2.4. HONO measurement and calibration

A time-of-flight chemical ionization mass spectrometer (ToF-CIMS, Aerodyne Inc.) was adopted to measure HONO concentrations in our laboratory experiments. The same instrument was described in our previous paper.[31] In this study, we used iodide and its water clusters as reagent ions to measure HONO concentrations. The reagent ions were generated by passing methyl iodide (CH_3I) gas through an ionizer (^{210}Po, NRD Corp.), and HONO was detected as $IHONO^-$ at 173.905 m/z (Fig. S1). All $IHONO^-$ signals were normalized to one million counts per second (cps) of primary ions before further analysis. High-resolution peak fitting found no/very minor spectral interference for HONO measurements. The sensitivity of HONO measurements by ToF-CIMS was calibrated before commencing the experiments. A HONO generator (QUMA, Model QS-03) produced a stable airflow containing HONO, which was then directed into both the ToF-CIMS and a long-path photochemical absorption photometer (LOPAP, QUMA Elektronik & Analytic GmbH). The LOPAP was pre-calibrated to obtain HONO concentrations used in the ToF-CIMS calibration. The sensitivity of the ToF-CIMS for HONO concentrations (3.07 to 1.42 cps ppt^{-1}) was found to be dependent on the RH (21.4% to 48.1%) of the HONO-containing air (Fig. S2). The instrument background of HONO (48.6 ± 1.0 ppt) was determined by injecting zero air into the ToF-CIMS.

3. Results and Discussion

3.1. HONO production during the irradiation experiment

A typical time series depicting the observed concentrations of HONO when aerosol filters were illuminated in the chamber is presented in Figure 2a. A rapid increase in HONO production was observed immediately after the chamber was illuminated, followed by an exponential decay. This pattern is consistent with previous filter-based experiments[13,16], suggesting that the HONO production was predominantly attributed to photochemical reactions of surface nitrate. The difference of measured HONO concentrations between two half filters in each NCP sample was less than 5% based on three sets of samples tested.

Upon the addition of the AM1.5 filter, the HONO concentration decreased by approximately 63% within 5 minutes and realigned with the exponential decay line upon removal of the filter. In contrast, the application of a 300–800 nm filter resulted in only a 17% reduction in HONO concentration, indicating that HONO production primarily occurred at wavelengths below 360 nm. This result aligns with previous studies, which indicate that HONO generation is primarily initiated in the long-wavelength range of UV light, peaking at 350 nm.[16,32] This observation may also suggest a redshift in the absorption wavelength of particulate nitrate,[23,24] resulting in a greater overlap between the xenon lamp irradiation and the particulate nitrate absorption spectrum compared to bulk aqueous nitrate. Although we cannot rule out the possibility of contribution from other nitrogen compounds, we assume that the HONO detected in the chamber was mainly produced from nitrate photolysis, similar to the viewpoint of a previous study[13]. We also investigated whether HONO production is affected by O_3, a crucial atmospheric oxidant. Our findings indicate that HONO production is independent of O_3, as evidenced by the sustained decay of HONO following the addition of 40-200 ppb of O_3 at different time of the experiments (Fig. 2a and Fig. S3).

Figure 3 presents the average P_{HONO} in different cities within the NCP region. The highest P_{HONO} (18×10^{-9} mol h^{-1}) was observed in a sample from Dezhou. The nitrate concentration in Dezhou was more than 13 times higher than that in Tianjin; however, the P_{HONO} in Dezhou was less than threefold that in Tianjin. This discrepancy indicates the presence of other influencing factors of nitrate photolysis besides nitrate concentration, such as the shadow effect or the nitrate distribution effect mentioned above.

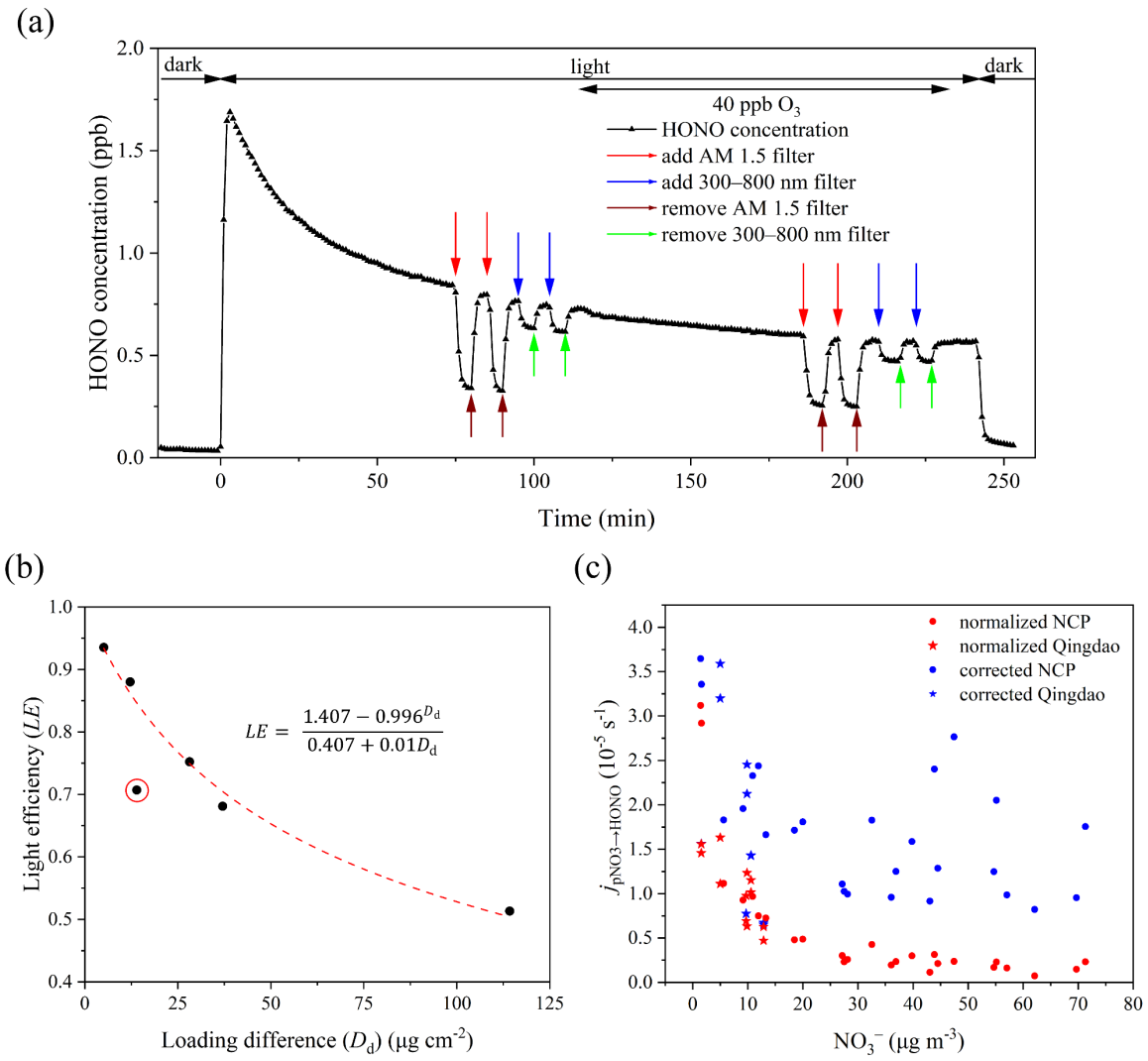

Figure 2. Results of laboratory experiments. (a) Typical pattern of HONO concentrations during irradiation (aerosols collected in Jinan on 3 Jan 2019). AM1.5 and 300–800 nm filters were added before and after adding 40 ppb O_3. (b) Light efficiency as a function of $PM_{2.5}$ loading difference. The red dashed line is the regression curve fitted using eq. 8. The data point in the red circle is an outlier. (c) Normalized $j_{pNO_3^- \rightarrow HONO}$ values (red) and corrected values (blue) of NCP (circles) and Qingdao (stars) shown as a function of nitrate concentration. Normalized $j_{pNO_3^- \rightarrow HONO}$ values are experimental values adjusted to tropical noontime conditions on the ground (solar zenith angle $\theta = 0°$). The corrected values are obtained by further adjusting the normalized values to account for the shadow effect.

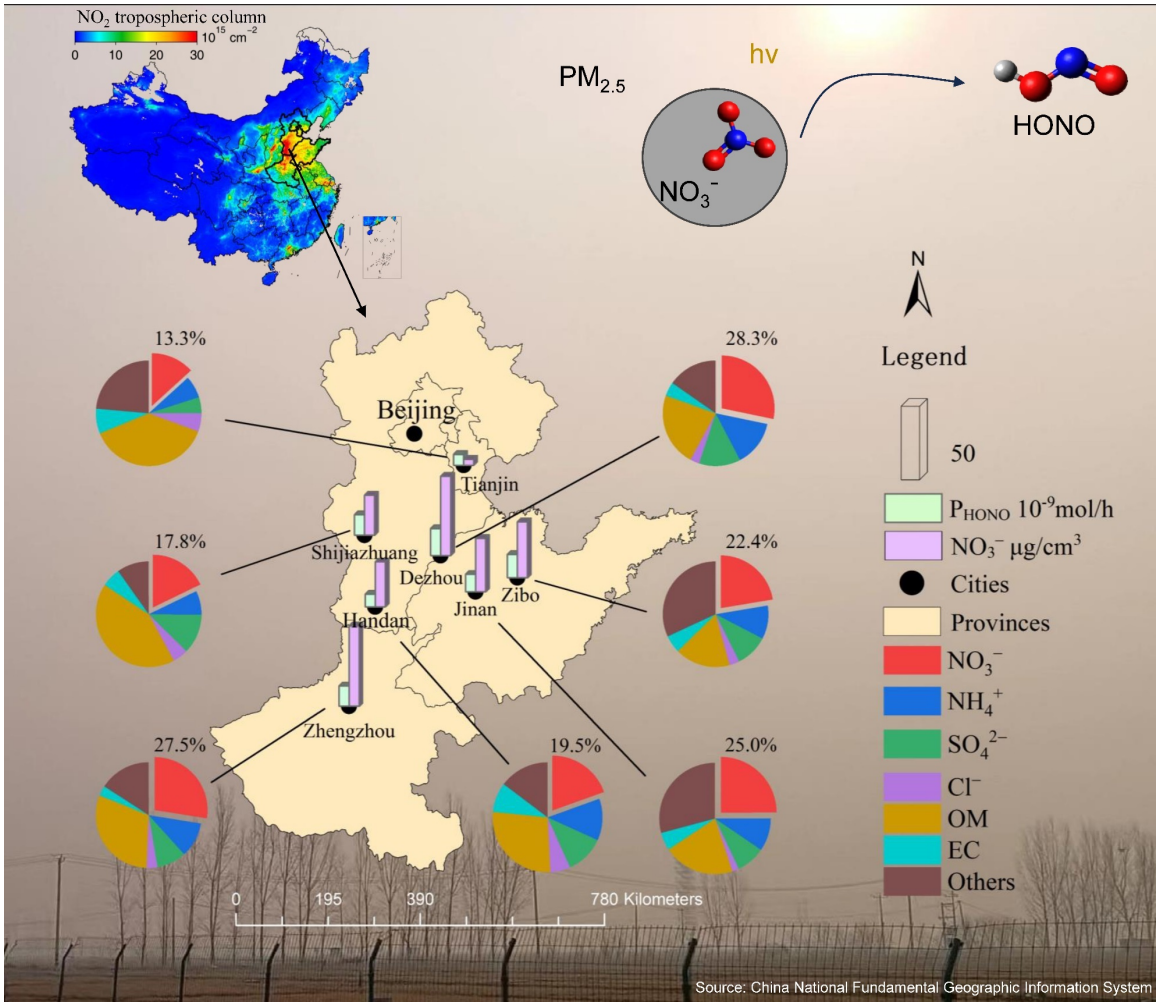

Figure 3. Spatial layout of the research area and average nitrate concentration (μg cm^{-3}), average HONO production rate (mol h^{-1}), and percentages of major $PM_{2.5}$ components in seven cities in the NCP. The upper left image presents the average NO_2 tropospheric column density from December 2018 to January 2019 across China, as derived from TROPOMI data.[33] The upper right image describes the process of photolysis of particulate nitrate producing HONO. The background photo was taken by the authors during a pollution episode at a rural site in the NCP. OM and EC represent organic matter and elemental carbon in $PM_{2.5}$, respectively. Geographic data sourced from the China National Fundamental Geographic Information System, National Geomatics Center of China, accessed in June, 2021.

Table 1. Summary of sample information and results of NCP filter experiments

Location	Sampling date	$PM_{2.5}$ loading ($\mu g\ cm^{-2}$)	Nitrate loading ($\mu mol\ cm^{-2}$)	$j_{pNO_3^- \rightarrow HONO}$ normalized ($10^{-6}\ s^{-1}$)	pH	Light efficiency (%)	$j_{pNO_3^- \rightarrow HONO}$ corrected ($10^{-6}\ s^{-1}$)
Zhengzhou	2017/12/27	346.11	1.55	2.28	3.81	11.12	20.51
	2018/11/27	223.36	1.01	1.96	3.56	20.46	9.59
	2019/1/4	276.55	1.96	1.47	3.78	15.45	9.54
Zibo	2017/12/2	236.73	1.12	2.98	3.50	18.78	15.86
	2017/12/27	172.73	0.79	2.58	3.60	26.00	9.93
	2017/12/28	314.06	1.23	3.13	3.88	13.03	24.01
Shijiazhuang	2019/1/1	166.18	0.56	4.86	3.40	26.90	18.07
	2019/1/3	236.55	1.04	2.35	3.37	18.80	12.49
	2019/1/4	158.56	0.52	4.80	3.37	28.00	17.14
	2019/1/9	106.13	0.31	9.67	3.22	41.56	23.28
	2019/1/12	418.75	1.33	2.37	3.33	8.55	27.66
Tianjin	2019/1/4	25.88	0.04	31.19	2.42	85.52	36.46
	2019/1/6	84.63	0.26	9.27	3.04	47.39	19.56
	2019/1/7	22.58	0.05	29.20	2.44	87.00	33.56
Dezhou	2017/12/29	306.42	1.54	1.68	3.99	13.48	12.46
	2018/11/26	310.40	2.00	2.32	4.00	13.24	17.56
	2019/1/2	194.53	0.91	4.27	3.73	23.36	18.28
Jinan	2017/12/1	262.66	1.25	2.12	3.38	16.51	12.86
	2017/12/27	201.64	0.77	2.32	3.58	22.59	10.26
	2018/12/31	97.97	0.37	7.25	3.36	43.61	16.62
	2019/1/3	262.46	1.60	1.63	3.75	16.52	9.86
Handan	2017/12/2	284.80	1.74	0.72	4.08	8.78	8.21
	2017/12/27	223.13	1.21	1.15	3.86	12.55	9.15
	2017/12/30	102.93	0.34	7.49	3.80	30.73	24.38
	2019/1/2	116.45	0.76	3.02	3.74	27.27	11.07
	2019/1/5	40.42	0.16	11.16	3.16	60.98	18.29
Mean value		199.72	0.94	5.89	3.51	28.39	17.18

3.2. Results of the shadow effect experiment

A total of six pairs of comparative experiments were conducted, the results of which are presented in Table 2 and Figure 2b. The only key variable that affected the *LE* was the variation in particle loading difference between two samples in each comparative set (denoted as D_d), given that their chemical compositions were identical. Overall, the *LE*

diminished as the D_d increased. This decrease in *LE* can be attributed to the accumulation of particles, which impedes light's ability to penetrate aerosols on the filter. In our experiment, *LE* decreased to as low as 51.33%, indicating that the actual $j_{pNO_3^- \rightarrow HONO}$ was about twice the value initially calculated. To represent the accumulation of particles on the filters, we established a model as illustrated in Figure 4a. In this model, particles on the filter are presumed to be evenly distributed and accumulated in multiple layers, similar to a layered cake. Accumulation in the second layer commences only after the complete coverage of the first layer, marking the onset of the shadow effect. In the first experiment (AH1 and AL1), the *LE* was measured as 93.53%, nearly approaching 100%, suggesting that AL1 was composed almost entirely of a single layer of particles. The $PM_{2.5}$ loading of AL1 represents the particle loading for one layer and the threshold for the initiation of shadow effect, referred to as D_s (12.82 μg cm^{-2}). This D_s value is consistent with the value from theoretical calculations (11.75 μg cm^{-2}) which is obtained by dividing the filter area by the cross-sectional area of a single particle (Text S3). We note that there is an outlier circled in red in Figure 2b, which is obtained from the BH1/BL1 experiment. The particle loading of BL1 (7.77 μg cm^{-2}, Table 2) is well below D_s, therefore the particulate matter on BL1 was insufficient to form a monolayer and thus not subject to the shadow effect. For this reason, this data point was not used in fitting the *LE* curve.

Table 2. Summary of sample information and results of the shadow effect experiment [a]

Sample No.	$PM_{2.5}$ loading (μg cm^{-2})	Nitrate loading (nmol cm^{-2})	P_{HONO} (nmol h^{-1})	Light efficiency (%)	$j_{pNO_3^- \rightarrow HONO}$ corrected (10^{-6} s^{-1})
AH1	17.92	25.21	3.48	93.53	15.59
AL1	12.82	18.04	2.68		
AH2	42.86	85.32	8.19	88.01	14.30
AL2	30.67	61.05	6.70		
AH3	130.31	242.14	25.48	68.10	33.94
AL3	93.25	173.27	26.91		
BH1	21.72	78.29	5.13	70.71	8.76
BL1	7.77	28.01	2.68		
BH2	43.88	211.22	9.44	75.22	6.63
BL2	15.70	75.57	4.51		
BH3	177.87	477.02	28.62	51.33	22.89
BL3	63.64	170.67	20.06		

[a] Set A was sampled at a flow rate of 1130 Lpm and 100 Lpm, while Set B was sampled at

1130 Lpm and 50 Lpm. Sampling durations were 3 h, 6 h, and 18 h, with samples labeled as follows: AH1-3 (high-volume, Set A), AL1-3 (low-volume, Set A), BH1-3 (high-volume, Set B), and BL1-3 (low-volume, Set B).

The aerosol filter samples collected from across the NCP can be regarded as multi-layered structures, as their $PM_{2.5}$ loadings were much larger than D_s. Therefore, the $j_{pNO_3^-\rightarrow HONO}$ initially calculated using eq. 2 was underestimated for these multi-layered samples. To rectify this, an adjustment of $j_{pNO_3^-\rightarrow HONO}$ to a single-layer equivalent was necessary. We first needed to establish a fundamentally sound formula that accurately models the relationship between *LE* and D_d. Assuming that the additional loading beyond the first layer (D_x) can be represented as multiple layers of D_s (i.e., $D_x = n \times D_s$, where n is the number of layers, ranging from 2 to 39 in this study), the *LE* of NCP samples can be calculated by eq. 4. To establish the relationship between $P_{HONO\text{-}x}$ and D_x, we assumed that the ratio of P_{HONO} between two adjacent layers was a constant, denoted as γ, in accordance with the Beer–Lambert law which describes the exponential decrease of light intensity as it propagates through a uniform medium (Text S4). Under this assumption, a geometric sequence expressed as eq. 5 was formulated. The cumulative $P_{HONO\text{-}x}$ can be calculated as the sum of $P_{HONO\text{-}xi}$, where $P_{HONO\text{-}xi}$ represents the P_{HONO} in the *i*th layer (eq. 6). The resulting expression for *LE* incorporating three constant parameters is shown in eq. 7. This expression was further simplified to eq. 8 by considering the boundary condition when D_x equals zero. Although D_d equals D_x only when the filter with lower particle loading in the comparative set consists of a single layer, applying eq. 8 to fit the data points in Figure 2b resulted in a high correlation coefficient ($R^2 = 0.99$) after excluding one outlier. The derived fitting parameters were $a = 1.407$, $b = 0.996$, $c = 0.010$. The fitting curve also captures the decreasing trend of *LE* as D_d increases, and it aligns with the theoretical inverse proportional decay pattern as D_d approaches infinity.

$$LE = \frac{j_{sample}}{j_s} = \frac{\frac{P_{HONO-s}+P_{HONO-x}}{n_{NO_3^--s}+n_{NO_3^--x}}}{\frac{P_{HONO-s}}{n_{NO_3^--s}}} = \frac{1+\frac{P_{HONO-x}}{P_{HONO-s}}}{1+\frac{n_{NO_3^--x}}{n_{NO_3^--s}}} \quad (4)$$

where $n_{NO_3^--s}$, $P_{HONO\text{-}s}$, and j_s are the nitrate abundance, HONO production rate, and the nitrate photolysis rate constant of the first layer, respectively. The same nomenclature is applied to the remaining part, represented as x.

$$P_{HONO-x_1} = \gamma \times P_{HONO-s}; P_{HONO-x_2} = \gamma \times P_{HONO-x_1}; \dots; P_{HONO-x_n} = \gamma \times P_{HONO-x_{n-1}} \quad (5)$$

$$P_{HONO-x} = \sum_{i=1}^{n} P_{HONO-x_i} = P_{HONO-s} \times \frac{\gamma-\gamma^{n+1}}{1-\gamma} \quad (6)$$

$$LE = \frac{1+\frac{\gamma-\gamma^{n+1}}{1-\gamma}}{1+n} = \frac{1-\gamma^{\frac{D_x}{D_s}+1}}{(1+\frac{D_x}{D_s})(1-\gamma)}$$, γ and D_s are constants (7)

$$LE = \frac{a-b^{D_x}}{a-1+c\times D_x} \quad (8)$$

The revised $j_{pNO_3^- \rightarrow HONO}$ obtained using this fitting equation remained underestimated in cases of high $PM_{2.5}$ loading, because the filter with lower particle loading in each pair of comparative experiments may have already exhibited the shadow effect, necessitating further correction toward a single-layer representation. Direct correction to a single layer is, however, impractical. Consequently, a dichotomous approach was adopted to iteratively refine the $j_{pNO_3^- \rightarrow HONO}$ estimation for multi-layered NCP filters. This method facilitated a stepwise approximation of the true value, as depicted in Figure 4b. The correction procedure involved calculating the *LE* for half the initial $PM_{2.5}$ loading using eq. 8, and then iteratively halving the $PM_{2.5}$ loading until it reached a point where further division would not result in a single layer (i.e., when D_s < $PM_{2.5}$ loading < $2D_s$). In this way, the actual *LE* was equivalent to the cumulative product of these iteratively calculated *LE*s, as shown in Table 1, and the $j_{pNO_3^- \rightarrow HONO}$ was recalculated by dividing by the actual *LE*. This revised method was initially employed to adjust the $j_{pNO_3^- \rightarrow HONO}$ values in the shadow effect experiments and yielded promising results: post-correction, the $j_{pNO_3^- \rightarrow HONO}$ under high aerosol loadings in each pair of parallel shadow effect experiments increased and aligned more closely with those under low aerosol loadings (Fig. 2c and Fig. S4).

We then applied the *LE* equation derived from the Qingdao samples to adjust the $j_{pNO_3^- \rightarrow HONO}$ values for samples from other cities in the NCP region. We noted that uncertainties may arise from such extrapolations, as the aerosol samples were collected from different cities and in different years (2017 vs 2022), although the ionic compositions of $PM_{2.5}$ in Qingdao are generally similar to those from other NCP cities (e.g., $R_{NO_3^-}$ is 16.9% compared with 20.8% in the NCP). The corrected $j_{pNO_3^- \rightarrow HONO}$ values for the NCP varied from 8.21×10^{-6} s^{-1} to 3.65×10^{-5} s^{-1}, with an average of 1.72×10^{-5} s^{-1}, significantly higher than the uncorrected mean value of 5.89×10^{-6} s^{-1}. The difference between the corrected and uncorrected $j_{pNO_3^- \rightarrow HONO}$ increases with higher aerosol loading (Fig. S5), confirming that the shadow effect is a factor contributing to the observed decrease in uncorrected $j_{pNO_3^- \rightarrow HONO}$ with increasing nitrate loading on filters.[13,16]

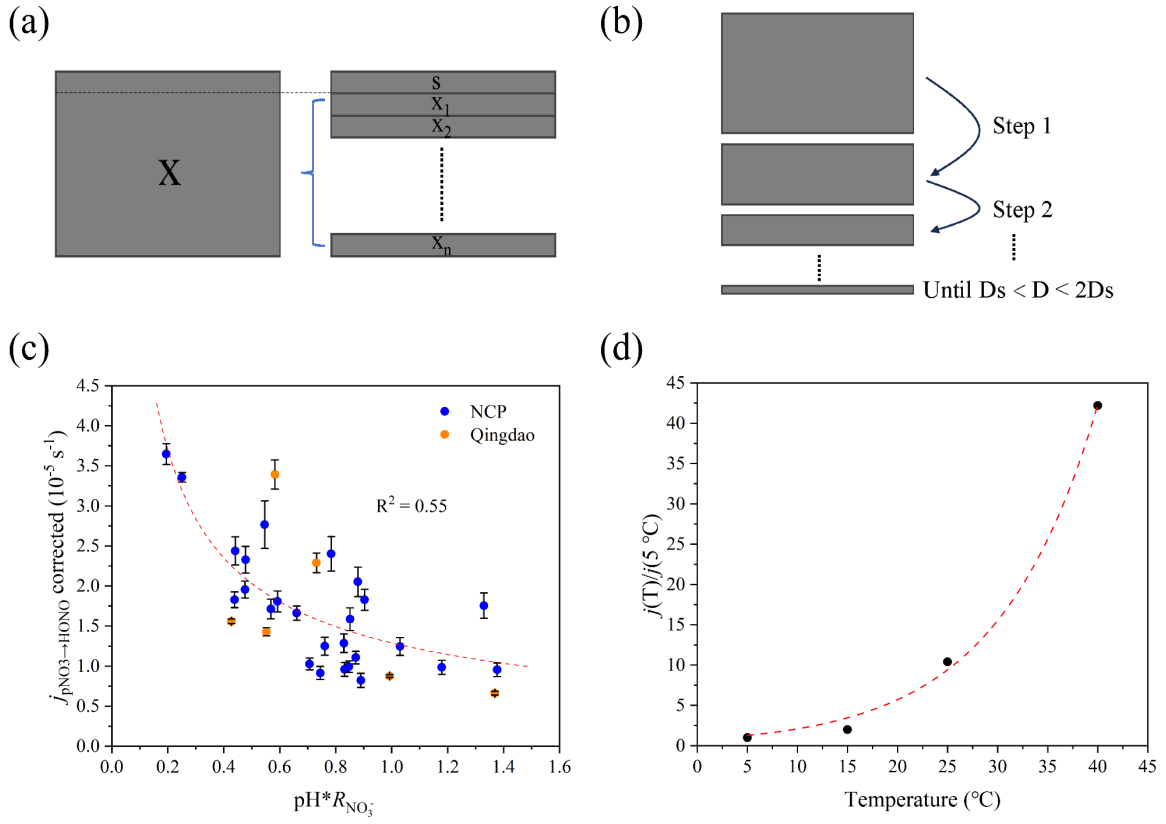

Figure 4. Principle of quantifying the influence of shadow effect and parameterization of corrected $j_{\mathrm{pNO_3^-}\rightarrow\mathrm{HONO}}$. (a) Schematic diagram of our model representing the accumulation of particles on filters, and (b) dichotomy method of stepwise approximation of the true $j_{\mathrm{pNO_3^-}\rightarrow\mathrm{HONO}}$. (c) Correlation between the corrected $j_{\mathrm{pNO_3^-}\rightarrow\mathrm{HONO}}$ and the product of pH and the proportion of NO_3^- in $PM_{2.5}$. The error bars are the errors propagated from the *LE* fitting curve (Text S5). (d) Dependence of $j_{\mathrm{pNO_3^-}\rightarrow\mathrm{HONO}}$ on temperature. The vertical axis shows the ratio of $j_{\mathrm{pNO_3^-}\rightarrow\mathrm{HONO}}$ at different temperatures to that at 5 °C. The data points were taken from Bao et al.[16] using WebPlotDigitizer (Version 4.6)[34].

3.3. Parameterization of $j_{\mathrm{pNO_3^-}\rightarrow\mathrm{HONO}}$

Pearson correlation coefficients were calculated for correlations between the corrected $j_{\mathrm{pNO_3^-}\rightarrow\mathrm{HONO}}$ and major chemical components in $PM_{2.5}$, including water-soluble ions and H^+ (Table S3). The H^+ concentrations were estimated using the Extended Aerosol Inorganic Model IV (E-AIM IV) (Text S2). The results revealed a significant negative correlation between the corrected $j_{\mathrm{pNO_3^-}\rightarrow\mathrm{HONO}}$ and $R_{\mathrm{NO_3^-}}$. A possible reason for this is the potential saturation effect under high particle loading conditions. Surface-adsorbed nitrate has a higher photolysis rate constant than bulk nitrate.[23] With surface-adsorbed nitrate approaching saturation, a further increase in $R_{\mathrm{NO_3^-}}$ would result in a lower proportion of

surface-adsorbed nitrate, resulting in a lower $j_{\mathrm{pNO_3^-\rightarrow HONO}}$ value when using total nitrate in the calculation. However, the exact reason for the decrease in $j_{\mathrm{pNO_3^-\rightarrow HONO}}$ values with $R_{\mathrm{NO_3^-}}$ requires further investigation. In addition to nitrate, aerosol acidity is another factor determining the $j_{\mathrm{pNO_3^-\rightarrow HONO}}$ values.[16,35,36] In this study, over 90% of the NCP samples had a pH in the range of 3–4, which is consistent with the pH estimated in other studies conducted in the NCP;[37–39] while samples from Qingdao demonstrated a lower acidity, with an average pH of 4.64. The corrected $j_{\mathrm{pNO_3^-\rightarrow HONO}}$ exhibited a pronounced negative correlation with pH, indicating the important role of H^+ in the formation of HONO. Given that both $R_{\mathrm{NO_3^-}}$ and pH are key factors controlling $j_{\mathrm{pNO_3^-\rightarrow HONO}}$, a parameterization considering both factors was developed by multiplying these two, resulting in a fitting equation (eq. 9) with an R^2 of 0.55, as shown in Figure 4c.

$$j_{\mathrm{pNO_3^-\rightarrow HONO}} = 1.29 \times 10^{-5} \times (\mathrm{pH} \times R_{\mathrm{NO_3^-}})^{-0.65} \quad (9)$$

where $R_{\mathrm{NO_3^-}}$ is the ratio of mass concentration of nitrate to $PM_{2.5}$.

To align our results with previous research, we accounted for the influence of temperature on $j_{\mathrm{pNO_3^-\rightarrow HONO}}$, as our experiments were conducted at 5 ℃ rather than at room temperature, as typically applied in prior studies. Bao et al.[16] investigated the impact of temperature on cumulative HONO production as a function of irradiation time over a range of 5 ℃ to 60 ℃. Figure 4d presents the relative ratio of HONO production at different temperatures to that at 5 ℃ (denoted as R_T) based on data from Bao et al. For consistency with our calculation methodology of HONO production (eq. 1), we selected data points at 15 min and excluded data recorded at 60 ℃, which is beyond the range of ambient temperatures in the troposphere. Generally, R_T exhibited an exponential increase with temperature in the range of 5 ℃ to 40 ℃, as demonstrated by eq. 10. While R_T remained approximately uniform at lower temperatures (< 15 ℃), R_T at 40 ℃ was larger than 40, demonstrating the remarkable influence of temperature on $j_{\mathrm{pNO_3^-\rightarrow HONO}}$. After normalizing our results to 20 ℃, the mean $j_{\mathrm{pNO_3^-\rightarrow HONO}}$ increased from 1.72×10^{-5} s^{-1} to 8.90×10^{-5} s^{-1}, which aligns with the mean value measured by Ye et al. in filter-based experiments in relatively clean environments (1.3×10^{-4} s^{-1}).[13] Bao et al. also obtained a comparable value in the polluted urban area of Beijing (8.24×10^{-5} s^{-1}), albeit a slight underestimation due to the shadow effect.

$$R_T = 0.77 \times 1.1^T \quad (10)$$

where R_T is ratio of HONO production at temperature T to that at 5 ℃; T is the temperature of the irradiation experiments (℃).

With the established relationship between $j_{\mathrm{pNO_3^-\rightarrow HONO}}$ and the three key factors pH, $R_{\mathrm{NO_3^-}}$, and temperature, we derived a parameterization for $j_{\mathrm{pNO_3^-\rightarrow HONO}}$, shown as eq. 11. The parameterization revealed that $j_{\mathrm{pNO_3^-\rightarrow HONO}}$ varied significantly across different

seasons (i.e., the temperature effect) and different aerosol compositions, especially nitrate content. Previous studies have found that particles with a lower pH tend to have a higher $j_{\mathrm{pNO_3^-\rightarrow HONO}}$,[40,41] which was also observed in our study and fundamentally supported by the participation of protons during the production of HONO. The $j_{\mathrm{pNO_3^-\rightarrow HONO}}$ is also affected by RH.[16,17,19] Bao et al. [16] found that $j_{\mathrm{pNO_3^-}}$ was relatively low under dry conditions (~3% RH), but it increased with RH, with minimal variation across intermediate RH levels (15%–75%). However, Sommariva et al.[18] observed a significantly higher value at RH levels of 75%–85% than at 24%, suggesting complex interactions between RH and nitrate photolysis. In view of these inconsistent results, RH has not been incorporated into the current parameterization. Further research is necessary to comprehensively understand the impact of humidity on nitrate photolysis.

$$j_{\mathrm{HNO3\rightarrow HONO}} = 1.0 \times 10^{-5} \times (\mathrm{pH} \times R_{\mathrm{NO_3^-}})^{-0.65} \times 1.1^{T} \quad (11)$$

3.4. Atmospheric implications

Our results demonstrated that the shadow effect can lead to a significant underestimation of $j_{\mathrm{pNO_3^-\rightarrow HONO}}$ measured with the filter-based method under high aerosol loading conditions. After correcting for the shadow effect, the average $j_{\mathrm{pNO_3^-\rightarrow HONO}}$ of NCP samples in winter was 1.72×10^{-5} s^{-1}. The $j_{\mathrm{pNO_3^-\rightarrow HONO}}$ is dependent on $R_{\mathrm{NO_3^-}}$ rather than on nitrate concentrations. Our results can help improve the modeling of HONO formation in NCP and other regions with similar chemical conditions. In current air-quality models, the $j_{\mathrm{pNO_3^-}}$ values employed at noontime tropical conditions are typically treated as constants (see Table S4, which compiles the $j_{\mathrm{pNO_3^-}}$ values applied in 12 studies conducted in China and the United States). Some of these studies adopted the maximum value (2.1×10^{-5} s^{-1}) reported by Romer et al. based on an assessment of the nitric acid budget, while others opted for the median (8.3×10^{-5} s^{-1}) or mean (1.3×10^{-4} s^{-1}) value sourced from Ye et al., who included filter-based experimental results for aerosols collected from various environments. However, there are no clear specific selection criteria for the $j_{\mathrm{pNO_3^-}}$ value applied in models. The large discrepancies in the applied $j_{\mathrm{pNO_3^-}}$ values in studies have undoubtedly impacted the estimation of HONO production rates from nitrate photolysis. The parameterization in our study, which accounts for variations in aerosol pH, $R_{\mathrm{NO_3^-}}$, and temperature, can reduce uncertainties in the $j_{\mathrm{pNO_3^-\rightarrow HONO}}$ predictions, thereby improving estimations of HONO budget and HONO impact on secondary pollutants.

We acknowledge that the parametrization developed in this study does not consider all factors that may influence the production of HONO from nitrate photolysis, as evidenced by the variance in the data points around the fitting line of the parameterization

(Fig. 4c). Besides the RH effect previously discussed, the presence of co-existing chemical species also affects the $j_{\mathrm{pNO_3^-\rightarrow HONO}}$. Inorganic species such as cations and halides have been shown to augment nitrate photolysis, whereas the impact of organic species is more nuanced; certain compounds, like oxalate and succinic acid, inhibit nitrate photolysis, whereas others, including photosensitizers, organic acids, and aromatic compounds, can facilitate it.[18,36] Therefore, the direct application of our parameterization to other environments should be done with caution. Future research incorporating global sample collection will be essential to validate and refine the shadow effect correction method and to adjust the parameterization to accommodate more diverse environmental conditions.

Supporting Information

Additional details on the determination of j_{HONO} and j_{exp}, settings of E-AIM IV, calculation of one-layer-particle loading, justification for applying the Beer–Lambert law in P_{HONO} analysis, calculation of the error for the corrected $j_{\mathrm{pNO_3^-\rightarrow HONO}}$ (Text S1–S5); chemical components of $PM_{2.5}$ samples, previously reported $j_{\mathrm{pNO_3^-}}$ values, Pearson correlation analysis, compilation of $j_{\mathrm{pNO_3^-}}$ applied in different modeling studies (Tables S1–S4); CIMS average spectra, the dependence of HONO sensitivity on RH, additional experiments of ozone effect on HONO production, the performance of correction method on Qingdao samples, correction factor of $j_{\mathrm{pNO_3^-\rightarrow HONO}}$ as a function of ambient $PM_{2.5}$ concentration, sensitivity test of E-AIM IV and normalized particle size distribution (Figures S1–S7).

Author Information

Corresponding Authors

Tao Wang − *Department of Civil and Environmental Engineering, The Hong Kong Polytechnic University, Hong Kong 999077, China*; Email: tao.wang@polyu.edu.hk

Jian Gao − *State Key Laboratory of Environmental Criteria and Risk Assessment, Chinese Research Academy of Environmental Sciences, Beijing, 100012, China*; Email: gaojian@craes.org.cn

Authors

Yifan Jiang − *Department of Civil and Environmental Engineering, The Hong Kong Polytechnic University, Hong Kong 999077, China*

Men Xia − *Department of Civil and Environmental Engineering, The Hong Kong*

Polytechnic University, Hong Kong 999077, China; Institute for Atmospheric and Earth System Research/Physics, Faculty of Science, University of Helsinki, Helsinki, 00014, Finland; Aerosol and Haze Laboratory, Advanced Innovation Center for Soft Matter Science and Engineering, Beijing University of Chemical Technology, 100029, Beijing, China

Likun Xue − *Environment Research Institute, Shandong University, Qingdao, 266237, China*

Xinfeng Wang − *Environment Research Institute, Shandong University, Qingdao, 266237, China*

Xuelian Zhong − *Environment Research Institute, Shandong University, Qingdao, 266237, China*

Yongchun Liu − *Aerosol and Haze Laboratory, Advanced Innovation Center for Soft Matter Science and Engineering, Beijing University of Chemical Technology, 100029, Beijing, China*

Markku Kulmala − *Institute for Atmospheric and Earth System Research/Physics, Faculty of Science, University of Helsinki, Helsinki, 00014, Finland; Aerosol and Haze Laboratory, Advanced Innovation Center for Soft Matter Science and Engineering, Beijing University of Chemical Technology, 100029, Beijing, China*

Tong Ma − *State Key Laboratory of Environmental Criteria and Risk Assessment, Chinese Research Academy of Environmental Sciences, Beijing, 100012, China*

Jiaqi Wang − *State Key Laboratory of Environmental Criteria and Risk Assessment, Chinese Research Academy of Environmental Sciences, Beijing, 100012, China*

Yurun Wang − *Department of Civil and Environmental Engineering, The Hong Kong Polytechnic University, Hong Kong 999077, China*

Author Contributions

TW designed the photochemical experiment. JG, TM and JW collected the 2018 and 2019 NCP filters and provided the sampling and IC data. LX, XW, XZ and YJ collected filters and auxiliary data in Qingdao. YJ and MX conducted the photochemical experiment of NCP filters. YJ conducted the shadow effect experiment, analyzed the data and draft the paper. TW and MX revised the paper with contributions from all authors.

Notes

The authors declare that they have no conflict of interests.

Acknowledgment

This work was supported by the Research Grants Council of Hong Kong (Project No. T24-504/17-N and 15207421) and National Key Research and Development Program of China (2022YFC3701100).

References

1. Acker, K.; Möller, D.; Wieprecht, W.; Meixner, F. X.; Bohn, B.; Gilge, S.; Plass-Dülmer, C.; Berresheim, H. Strong Daytime Production of OH from HNO2 at a Rural Mountain Site. Geophys. Res. Lett. 2006, 33 (2), L02809. https://doi.org/10.1029/2005GL024643.
2. Alicke, B.; Geyer, A.; Hofzumahaus, A.; Holland, F.; Konrad, S.; Pätz, H. W.; Schäfer, J.; Stutz, J.; Volz-Thomas, A.; Platt, U. OH Formation by HONO Photolysis during the BERLIOZ Experiment. J. Geophys. Res.: Atmos. 2003, 108 (D4), 8247. https://doi.org/10.1029/2001JD000579.
3. Kim, S.; VandenBoer, T. C.; Young, C. J.; Riedel, T. P.; Thornton, J. A.; Swarthout, B.; Sive, B.; Lerner, B.; Gilman, J. B.; Warneke, C.; Roberts, J. M.; Guenther, A.; Wagner, N. L.; Dubé, W. P.; Williams, E.; Brown, S. S. The Primary and Recycling Sources of OH during the NACHTT-2011 Campaign: HONO as an Important OH Primary Source in the Wintertime. J. Geophys. Res.: Atmos. 2014, 119 (11), 6886–6896. https://doi.org/10.1002/2013JD019784.
4. Yun, H.; Wang, Z.; Zha, Q.; Wang, W.; Xue, L.; Zhang, L.; Li, Q.; Cui, L.; Lee, S.; Poon, S. C. N.; Wang, T. Nitrous Acid in a Street Canyon Environment: Sources and Contributions to Local Oxidation Capacity. Atmos. Environ. 2017, 167, 223–234. https://doi.org/10.1016/j.atmosenv.2017.08.018.
5. Kleffmann, J.; Gavriloaiei, T.; Hofzumahaus, A.; Holland, F.; Koppmann, R.; Rupp, L.; Schlosser, E.; Siese, M.; Wahner, A. Daytime Formation of Nitrous Acid: A Major Source of OH Radicals in a Forest. Geophys. Res. Lett. 2005, 32 (5), L05818. https://doi.org/10.1029/2005GL022524.
6. Fu, X.; Wang, T.; Zhang, L.; Li, Q.; Wang, Z.; Xia, M.; Yun, H.; Wang, W.; Yu, C.; Yue, D.; Zhou, Y.; Zheng, J.; Han, R. The Significant Contribution of HONO to Secondary Pollutants during a Severe Winter Pollution Event in Southern China. Atmos. Chem. Phys. 2019, 19 (1), 1–14. https://doi.org/10.5194/acp-19-1-2019.
7. Wang, T.; Xue, L.; Feng, Z.; Dai, J.; Zhang, Y.; Tan, Y. Ground-Level Ozone Pollution in China: A Synthesis of Recent Findings on Influencing Factors and

Impacts. Environ. Res. Lett. 2022, 17 (6), 063003. https://doi.org/10.1088/1748-9326/ac69fe.

8. Wang, Y.; Fu, X.; Wu, D.; Wang, M.; Lu, K.; Mu, Y.; Liu, Z.; Zhang, Y.; Wang, T. Agricultural Fertilization Aggravates Air Pollution by Stimulating Soil Nitrous Acid Emissions at High Soil Moisture. Environ. Sci. Technol. 2021, 55 (21), 14556–14566. https://doi.org/10.1021/acs.est.1c04134.
9. Liu, Y.; Lu, K.; Ma, Y.; Yang, X.; Zhang, W.; Wu, Y.; Peng, J.; Shuai, S.; Hu, M.; Zhang, Y. Direct Emission of Nitrous Acid (HONO) from Gasoline Cars in China Determined by Vehicle Chassis Dynamometer Experiments. Atmos. Environ. 2017, 169, 89–96. https://doi.org/10.1016/j.atmosenv.2017.07.019.
10. Yokelson, R. J.; Karl, T.; Artaxo, P.; Blake, D. R.; Christian, T. J.; Griffith, D. W. T.; Guenther, A.; Hao, W. M. The Tropical Forest and Fire Emissions Experiment: Overview and Airborne Fire Emission Factor Measurements. Atmos. Chem. Phys. 2007, 7 (19), 5175–5196. https://doi.org/10.5194/acp-7-5175-2007.
11. Pagsberg, P.; Bjergbakke, E.; Ratajczak, E.; Sillesen, A. Kinetics of the Gas Phase Reaction OH + NO(+M)→HONO(+M) and the Determination of the UV Absorption Cross Sections of HONO. Chem. Phys. Lett. 1997, 272 (5–6), 383–390. https://doi.org/10.1016/S0009-2614(97)00576-9.
12. Kleffmann, J.; Benter, T.; Wiesen, P. Heterogeneous Reaction of Nitric Acid with Nitric Oxide on Glass Surfaces under Simulated Atmospheric Conditions. J. Phys. Chem. A 2004, 108 (27), 5793–5799. https://doi.org/10.1021/jp040184u.
13. Ye, C.; Zhang, N.; Gao, H.; Zhou, X. Photolysis of Particulate Nitrate as a Source of HONO and NOx. Environ. Sci. Technol. 2017, 51 (12), 6849–6856. https://doi.org/10.1021/acs.est.7b00387.
14. Benedict, K. B.; McFall, A. S.; Anastasio, C. Quantum Yield of Nitrite from the Photolysis of Aqueous Nitrate above 300 Nm. Environ. Sci. Technol. 2017, 51 (8), 4387–4395. https://doi.org/10.1021/acs.est.6b06370.
15. Ye, C.; Zhou, X.; Pu, D.; Stutz, J.; Festa, J.; Spolaor, M.; Tsai, C.; Cantrell, C.; Mauldin, R. L.; Campos, T.; Weinheimer, A.; Hornbrook, R. S.; Apel, E. C.; Guenther, A.; Kaser, L.; Yuan, B.; Karl, T.; Haggerty, J.; Hall, S.; Ullmann, K.; Smith, J. N.; Ortega, J.; Knote, C. Rapid Cycling of Reactive Nitrogen in the Marine Boundary Layer. Nature 2016, 532, 489–491. https://doi.org/10.1038/nature17195.
16. Bao, F.; Li, M.; Zhang, Y.; Chen, C.; Zhao, J. Photochemical Aging of Beijing Urban PM2.5: HONO Production. Environ. Sci. Technol. 2018, 52 (11), 6309–6316. https://doi.org/10.1021/acs.est.8b00538.
17. Andersen, S. T.; Carpenter, L. J.; Reed, C.; Lee, J. D.; Chance, R.; Sherwen, T.;

Vaughan, A. R.; Stewart, J.; Edwards, P. M.; Bloss, W. J.; Sommariva, R.; Crilley, L. R.; Nott, G. J.; Neves, L.; Read, K.; Heard, D. E.; Seakins, P. W.; Whalley, L. K.; Boustead, G. A.; Fleming, L. T.; Stone, D.; Fomba, K. W. Extensive Field Evidence for the Release of HONO from the Photolysis of Nitrate Aerosols. Sci. Adv. 2023, 9 (3), eadd6266. https://doi.org/10.1126/sciadv.add6266.

18. Sommariva, R.; Alam, M. S.; Crilley, L. R.; Rooney, D. J.; Bloss, W. J.; Fomba, K. W.; Andersen, S. T.; Carpenter, L. J. Factors Influencing the Formation of Nitrous Acid from Photolysis of Particulate Nitrate. J. Phys. Chem. A 2023, 127 (44), 9302–9310. https://doi.org/10.1021/acs.jpca.3c03853.
19. Shi, Q.; Tao, Y.; Krechmer, J. E.; Heald, C. L.; Murphy, J. G.; Kroll, J. H.; Ye, Q. Laboratory Investigation of Renoxification from the Photolysis of Inorganic Particulate Nitrate. Environ. Sci. Technol. 2021, 55 (2), 854–861. https://doi.org/10.1021/acs.est.0c06049.
20. Romer, P. S.; Wooldridge, P. J.; Crounse, J. D.; Kim, M. J.; Wennberg, P. O.; Dibb, J. E.; Scheuer, E.; Blake, D. R.; Meinardi, S.; Brosius, A. L.; Thames, A. B.; Miller, D. O.; Brune, W. H.; Hall, S. R.; Ryerson, T. B.; Cohen, R. C. Constraints on Aerosol Nitrate Photolysis as a Potential Source of HONO and NOx. Environ. Sci. Technol. 2018, 52 (23), 13738–13746. https://doi.org/10.1021/acs.est.8b03861.
21. Zhu, Y.; Wang, Y.; Zhou, X.; Elshorbany, Y. F.; Ye, C.; Hayden, M.; Peters, A. J. An Investigation into the Chemistry of HONO in the Marine Boundary Layer at Tudor Hill Marine Atmospheric Observatory in Bermuda. Atmos. Chem. Phys. 2022, 22 (9), 6327–6346. https://doi.org/10.5194/acp-22-6327-2022.
22. Kasibhatla, P.; Sherwen, T.; Evans, M. J.; Carpenter, L. J.; Reed, C.; Alexander, B.; Chen, Q.; Sulprizio, M. P.; Lee, J. D.; Read, K. A.; Bloss, W.; Crilley, L. R.; Keene, W. C.; Pszenny, A. A. P.; Hodzic, A. Global Impact of Nitrate Photolysis in Sea-Salt Aerosol on NOx, OH, and O3 in the Marine Boundary Layer. Atmos. Chem. Phys. 2018, 18 (15), 11185–11203. https://doi.org/10.5194/acp-18-11185-2018.
23. Zhu, C.; Xiang, B.; Zhu, L.; Cole, R. Determination of Absorption Cross Sections of Surface-Adsorbed HNO3 in the 290-330 Nm Region by Brewster Angle Cavity Ring-down Spectroscopy. Chem. Phys. Lett. 2008, 458 (4–6), 373–377. https://doi.org/10.1016/j.cplett.2008.04.125.
24. Du, J.; Zhu, L. Quantification of the Absorption Cross Sections of Surface-Adsorbed Nitric Acid in the 335-365 Nm Region by Brewster Angle Cavity Ring-down Spectroscopy. Chem. Phys. Lett. 2011, 511 (4–6), 213–218. https://doi.org/10.1016/j.cplett.2011.06.062.
25. Wang, Y.; Gong, Z.; Liu, Z.; Tang, G.; Cheng, L.; Che, F.; Gao, J.; Ji, D.

Construction and Application of Comprehensive Observation Network for Air Pollution in Beijing-Tianjin-Hebei and Its Surrounding Areas. Res. Environ. Sci. 2019, 32 (10), 1651–1663. https://doi.org/10.13198/j.issn.1001-6929.2019.09.12.

26. Pang, N.; Gao, J.; Che, F.; Ma, T.; Liu, S.; Yang, Y.; Zhao, P.; Yuan, J.; Liu, J.; Xu, Z.; Chai, F. Cause of PM2.5 Pollution during the 2016-2017 Heating Season in Beijing, Tianjin, and Langfang, China. J. Environ. Sci. (China) 2020, 95, 201–209. https://doi.org/10.1016/j.jes.2020.03.024.
27. Huang, X.; Liu, Z.; Liu, J.; Hu, B.; Wen, T.; Tang, G.; Zhang, J.; Wu, F.; Ji, D.; Wang, L.; Wang, Y. Chemical Characterization and Source Identification of PM2.5 at Multiple Sites in the Beijing-Tianjin-Hebei Region, China. Atmos. Chem. Phys. 2017, 17 (21), 12941–12962. https://doi.org/10.5194/acp-17-12941-2017.
28. Zhang, Y. Q.; Wang, J.; Gao, J.; Xu, Z. J.; Che, F.; Ma, T.; Yang, Y.; Liu, S.; Yan, L. L. Chemical Composition Characteristics and Source Apportionment of PM2.5 During the Heating Period of 2016-2017 in the Eastern Part of the North China Plain. Huanjing Kexue/Environmental Science 2019, 40 (12), 5202–5212. https://doi.org/10.13227/j.hjkx.201904076.
29. Wang, J.; Zhang, Y. Q.; Gao, J.; Xu, Z. J.; Ma, T.; Liu, S.; Yan, L. L.; Liu, J. Y. Characteristics of PM2.5 in Cities along the Taihang Mountains during the Heating Season of 2016~2018. Zhongguo Huanjing Kexue/China Environmental Science 2019, 39 (11), 4521–4529. https://doi.org/10.19674/j.cnki.issn1000-6923.2019.0526.
30. Chu, L.; Anastasio, C. Quantum Yields of Hydroxyl Radical and Nitrogen Dioxide from the Photolysis of Nitrate on Ice. J. Phys. Chem. A 2003, 107 (45), 9594–9602. https://doi.org/10.1021/jp0349132.
31. Xia, M.; Wang, T.; Wang, Z.; Chen, Y.; Peng, X.; Huo, Y.; Wang, W.; Yuan, Q.; Jiang, Y.; Guo, H.; Lau, C.; Leung, K.; Yu, A.; Lee, S. Pollution-Derived Br2 Boosts Oxidation Power of the Coastal Atmosphere. Environ. Sci. Technol. 2022, 56 (17), 12055–12065. https://doi.org/10.1021/acs.est.2c02434.
32. Wang, Y.; Wang, J.; Wang, Y.; Zhang, Y.; Woodward-Massey, R.; Zhang, C.; Kuang, Y.; Zhu, J.; Shang, J.; Li, X.; Zeng, L.; Lin, W.; Ye, C. Experimental and Kinetic Model Evaluation of HONO Production from Surface Nitrate Photolysis. Atmos. Environ. 2023, 296, 119568. https://doi.org/10.1016/j.atmosenv.2022.119568.
33. Van Geffen, J.; Boersma, F. K.; Eskes, H.; Sneep, M.; Ter Linden, M.; Zara, M.; Veefkind, J. P. S5P TROPOMI NO2 Slant Column Retrieval: Method, Stability, Uncertainties and Comparisons with OMI. Atmos. Meas. Tech. 2020, 13 (3), 1315–1335. https://doi.org/10.5194/amt-13-1315-2020.

34. Rohatgi, A. WebPlotDigitizer: Version 4.6; 2022. Available online at https://automeris.io/WebPlotDigitizer.
35. Scharko, N. K.; Berke, A. E.; Raff, J. D. Release of Nitrous Acid and Nitrogen Dioxide from Nitrate Photolysis in Acidic Aqueous Solutions. Environ. Sci. Technol. 2014, 48 (20), 11991–12001. https://doi.org/10.1021/es503088x.
36. Gen, M.; Liang, Z.; Zhang, R.; Mabato, B. R. G.; Chan, C. K. Particulate Nitrate Photolysis in the Atmosphere. Environ. Sci.: Atmos. 2022, 2, 111–127. https://doi.org/10.1039/d1ea00087j.
37. Peng, X.; Vasilakos, P.; Nenes, A.; Shi, G.; Qian, Y.; Shi, X.; Xiao, Z.; Chen, K.; Feng, Y.; Russell, A. G. Detailed Analysis of Estimated PH, Activity Coefficients, and Ion Concentrations between the Three Aerosol Thermodynamic Models. Environ. Sci. Technol. 2019, 53 (15), 8903–8913. https://doi.org/10.1021/acs.est.9b00181.
38. Tan, T.; Hu, M.; Li, M.; Guo, Q.; Wu, Y.; Fang, X.; Gu, F.; Wang, Y.; Wu, Z. New Insight into PM2.5 Pollution Patterns in Beijing Based on One-Year Measurement of Chemical Compositions. Sci. Total Environ. 2018, 621, 734–743. https://doi.org/10.1016/j.scitotenv.2017.11.208.
39. Liu, M.; Song, Y.; Zhou, T.; Xu, Z.; Yan, C.; Zheng, M.; Wu, Z.; Hu, M.; Wu, Y.; Zhu, T. Fine Particle PH during Severe Haze Episodes in Northern China. Geophys. Res. Lett. 2017, 44 (10), 5213–5221. https://doi.org/10.1002/2017GL073210.
40. Scharko, N. K.; Berke, A. E.; Raff, J. D. Release of Nitrous Acid and Nitrogen Dioxide from Nitrate Photolysis in Acidic Aqueous Solutions. Environ. Sci. Technol. 2014, 48 (20), 11991–12001. https://doi.org/10.1021/ES503088X.
41. Bao, F.; Jiang, H.; Zhang, Y.; Li, M.; Ye, C.; Wang, W.; Ge, M.; Chen, C.; Zhao, J. The Key Role of Sulfate in the Photochemical Renoxification on Real PM2.5. Environ. Sci. Technol. 2020, 54 (6), 3121–3128. https://doi.org/10.1021/acs.est.9b06764.

Supplementary information for

Quantifying HONO Production from Nitrate Photolysis in a Polluted Atmosphere

Yifan Jiang[1]*, Men Xia[1,2,3]*, Likun Xue[4], Xinfeng Wang[4], Xuelian Zhong[4], Yongchun Liu[3], Markku Kulmala[2,3], Tong Ma[5], Jiaqi Wang[5], Yurun Wang[1], Jian Gao[5], and Tao Wang[1]

[1]Department of Civil and Environmental Engineering, The Hong Kong Polytechnic University, Hong Kong 999077, China

[2]Institute for Atmospheric and Earth System Research/Physics, Faculty of Science, University of Helsinki, Helsinki 00014, Finland

[3]Aerosol and Haze Laboratory, Advanced Innovation Center for Soft Matter Science and Engineering, Beijing University of Chemical Technology, Beijing 100029, China

[4]Environment Research Institute, Shandong University, Qingdao 266237, China

[5]State Key Laboratory of Environmental Criteria and Risk Assessment, Chinese Research Academy of Environmental Sciences, Beijing 100012, China

Correspondence to: Jian Gao (gaojian@craes.org.cn) and Tao Wang (tao.wang@polyu.edu.hk)

*These authors contributed equally to this work.

Summary of supporting information:

NO. OF TEXTS: 5

NO. OF TABLES: 4

NO. OF FIGURES: 7

NO. OF PAGES: 13

Table of contents

Text S1. Determination of the photolysis rate constant of HONO and nitrate under the irradiation of xenon lamp.

The photolysis rate constant of HONO and nitrate was calculated by eq 1.

$$j = \int q(\lambda)\sigma(\lambda)I(\lambda)\mathrm{d}\lambda \quad (1)$$

where $q(\lambda)$ is the quantum yield at wavelength λ (nm); $\sigma(\lambda)$ is the cross-section at wavelength λ; $I(\lambda)$ is the flux of xenon lamp at wavelength λ. The flux of the xenon lamp at wavelength λ was determined by converting the irradiation energy spectra of the lamp (see Fig. 1b) to photon flux using Planck's equation. The values of $q(\lambda)$ and σ(λ) of HONO was obtained from the recommended value provided by IUPAC at 278 K (http://iupac.pole-ether.fr/index.html). The $q(\lambda)$ and $\sigma(\lambda)$ of aqueous nitrate were derived from Chu et al.[1] It should be noted that the spectrum of aqueous nitrate photolysis should be different from particulate nitrate photolysis, resulting in some uncertainty when extrapolating to the ambient conditions.

Text S2. Settings of Extended Aerosol Inorganic Model IV (E-AIM IV) and sensitivity test of pH on NH_3 and RH input.

To estimate the acidity of aerosols on the filters, the E-AIM model IV (batch mode) was run online at http://www.aim.env.uea.ac.uk/aim/model4/model4a.php.[2] Here we assumed that the overall acidity of ambient aerosols did not change after they were collected on the filters. The RH measured in the chamber (50 ~ 55 %) and the daily air-born concentration of Na^+, NH_4^+, Cl^-, NO_3^-, and SO_4^{2-} (mol m^{-3}) were adopted as input. The initial molarity of H^+ was set to balance the total charges of anions and cations. For lack of ambient NH_3 data, we further assumed that the molarity of NH_3 equaled that of NH_4^+ and tested the sensitivity of acidity on NH_3 input. Parameter r was therefore set as 0 to allow NH_3 (g) can be formed and partition between the condensed and gas phases. Other model configuration was shown as follows. Parameter e = 1, which means that water dissociation was considered by the model. Parameters p, q, s were set as 3, which means that the input amount of NO_3^-, Cl^-, and SO_4^{2-} stay in the liquid or solid phase. Their gas-phase counterparts, i.e., HNO_3, HCl, and H_2SO_4, were calculated based on the gas-particle equilibrium. The parameter u was set as 0, which means all potential solids can form in the system.

To investigate the effect of NH_3 input on the acidity, we conducted a sensitivity test using different ratio of the concentration of NH_4^+ to that of NH_3 (Fig. S6a). The results show that the average pH increased from 3.45 ± 0.16 to 3.81 ± 0.16 when doubling the concentration of NH_3, while decreased to 2.85 ± 0.59 when halving the concentration of NH_3. The ambient NH_3 mass concentration is usually larger than or equivalent to the mass concentration of NH_4^+ in polluted areas.[3] We also conducted a sensitivity test on

RH input since the ambient RH will change and is different from the RH measured in the chamber (Fig. S6b). The acidity increases with RH when RH is lower than 0.7 and tends to be independent after that.

Text S3. Theoretical calculation of the loading of one-layer particles.

To preliminarily determine the mass density of particles with one layer, namely D_s, we assumed that all particles are spherical and were distributed uniformly and compactly. Based on the particle size distribution of Qingdao samples (Fig. S7), we determined the dominant particle diameter as 110.14 nm. Therefore, D_s can be calculated using the eq 2 assuming all particles are the same with the dominant particle size. The calculated D_s is 11.75 μg cm^{-2}, which is close to the value determined by the shadow effect experiments, 12.8 μg cm^{-2}, indicating that determination of D_s is reasonable.

$$D_s = \frac{V_p \rho_p}{S_p} \quad (2)$$

where S_p is the area of the cross section of a single particle (cm^2); V_p is the volume of a single particle (cm^3); ρ_p is the density of particles, here is assumed as 1.6 g cm^{-3}.

Text S4. Justification for applying the Beer–Lambert law in P_{HONO} Analysis.

In a uniform medium, light intensity decreases exponentially as it propagates through the medium, in accordance with the Beer-Lambert law. Assuming each layer has the same thickness, and the medium possesses a consistent absorption coefficient and concentration, the exponential form of the Beer-Lambert law can be expressed as eq 3.

$$I = I_0 e^{-\alpha \chi} \quad (3)$$

where I is the intensity of light after passing through the medium; I_0 is the incident light intensity; α is the absorption coefficient, which is related to the medium's molar absorptivity and concentration; χ is the distance the light travels through the medium.

For a single layer with thickness d, the light intensity after passing through the n-th layer, I_n, can be expressed as eq 4.

$$I_n = I_0 e^{-n\alpha d} \quad (4)$$

Therefore, the ratio of light intensities between adjacent layers (the n-th and the (n+1)-th layer) is a constant, as calculated in eq 5.

$$\frac{I_{n+1}}{I_n} = \frac{I_0 e^{-(n+1)\alpha d}}{I_0 e^{-n\alpha d}} = e^{-\alpha d} \quad (5)$$

Text S5. Calculation of the error for the $j_{pNO_3^- \rightarrow HONO}$ corrected using the LE fitting curve.

The errors in the LE directly affect the calculated $j_{pNO_3^- \rightarrow HONO}$ values. We

assume that the primary source of uncertainty in the calculated $j_{\mathrm{pNO_3^-\rightarrow HONO}}$ stems from the LE fitting curve. Since corrected $j_{\mathrm{pNO_3^-\rightarrow HONO}}$ values were divided by LE multiple times based on the dichotomous approach, the relative error of corrected $j_{\mathrm{pNO_3^-\rightarrow HONO}}$ values intensifies proportionally (eq 6).

$$\frac{\sigma_{j_c}}{j_c} = \mathrm{n}\frac{\sigma_{LE}}{LE} \quad (6)$$

where j_c represents the corrected $j_{\mathrm{pNO_3^-\rightarrow HONO}}$; σ_{j_c} is the standard error of j_c; n is the number of times division is applied using dichotomous approach, σ_{LE} is the standard error of LE, which was obtained from the LE fitting curve.

Supplementary Tables

Table S1. Chemical components of $PM_{2.5}$ samples in the North China Plain. [a]

Location	Date	$PM_{2.5}$	Na^+	K^+	NH_4^+	Mg^{2+}	Ca^{2+}	Cl^-	NO_3^-	SO_4^{2-}	OC	EC
Zhengzhou	2017/12/27	239.27	0.57	3.30	23.73	0.18	2.10	9.40	55.14	16.59	41.73	14.07
	2018/11/27	154.41	0.70	1.33	13.36	0.22	2.62	1.52	36.08	13.97	23.44	2.81
	2019/1/4	191.18	0.51	2.06	25.86	0.05	0.32	8.62	69.70	22.21	45.93	1.21
Zibo	2017/12/2	163.65	0.47	1.69	14.39	0.25	2.99	4.24	39.83	15.15	17.55	6.15
	2017/12/27	119.41	0.24	1.07	13.27	0.13	1.53	3.86	28.13	10.70	14.33	5.40
	2017/12/28	217.11	0.67	2.00	23.74	0.07	0.90	7.64	43.88	24.05	20.98	15.53
Shijiazhuang	2019/1/1	114.88	3.76	0.99	8.75	0.34	2.35	6.40	20.01	10.79	41.46	8.15
	2019/1/3	163.53	3.84	1.56	12.90	0.34	3.69	8.32	36.90	18.46	42.91	9.79
	2019/1/4	109.61	2.82	0.89	7.84	0.24	2.54	4.89	18.48	8.28	30.39	7.81
	2019/1/9	73.37	1.90	0.94	6.09	0.14	1.75	6.67	10.90	5.93	24.11	6.02
	2019/1/12	289.48	4.92	2.08	19.49	0.41	4.78	9.14	47.45	48.11	59.59	12.08
Tianjin	2019/1/4	17.89	0.25	0.06	0.95	0.11	0.64	0.44	1.44	1.04	3.34	0.93
	2019/1/6	58.51	0.58	0.57	4.31	0.15	0.97	4.33	9.16	2.48	13.51	4.96
	2019/1/7	15.61	0.23	0.12	1.00	0.09	0.58	0.44	1.60	0.98	5.09	1.15
Dezhou	2017/12/29	211.83	0.26	1.79	29.93	ND [b]	ND	5.47	54.69	33.50	19.29	5.34
	2018/11/26	214.58	0.31	2.42	32.34	0.07	0.42	3.40	71.33	25.76	30.35	10.83
	2019/1/2	134.48	0.60	1.92	16.69	0.09	0.39	7.30	32.55	11.84	29.34	7.86
Jinan	2017/12/1	181.58	0.48	1.54	13.67	0.34	5.29	2.64	44.53	15.43	20.28	6.83
	2017/12/27	139.39	0.29	1.08	12.39	0.31	5.42	2.79	27.52	9.79	15.04	9.44
	2018/12/31	67.73	0.28	0.42	7.15	0.09	1.00	2.53	13.30	5.08	10.67	3.97
	2019/1/3	181.44	0.62	1.45	21.23	0.14	1.61	3.25	57.06	17.96	27.69	9.32
Handan	2017/12/2	284.80	1.35	3.01	36.31	0.24	4.33	15.01	62.10	32.73	40.35	13.03
	2017/12/27	223.13	0.88	1.96	24.68	0.06	1.19	12.31	43.06	26.45	23.21	37.31
	2017/12/30	102.93	0.42	0.87	10.40	ND	1.00	5.76	11.95	14.31	23.23	7.66
	2019/1/2	116.45	0.67	2.39	17.57	0.22	2.45	8.36	27.17	12.12	32.62	5.90

2019/1/5	40.42	0.37	0.75	5.30	0.12	1.49	3.86	5.61	2.62	12.11	2.54

[a] All chemical components are measured in μg m^{-3}. [b] ND: not detectable.

Table S2. Summary of reported $j_{pNO_3^-}$ values in various environments.

Study type	$j_{pNO_3^-}$ (10^{-5} s^{-1})	Air mass origin	Reference
Laboratory	0.62–50 (13[a])	Remote, rural, urban	4
Laboratory	1.2–48 (8.2)[b]	Urban	5
Laboratory	0.1–1.8 (0.32)	Marine	6
Laboratory	1.3–31 (17)	Marine	7
Laboratory	<0.7[c]		8
Model	2.0[c]	Marine	6
Model	20[b]	Marine	7
Model	0.07–2.1[c]		9

[a] Values in parentheses are the average values. [b] $j_{pNO_3^-}$ here is the $j_{pNO_3^-}$ leading to HONO production. [c] Calculated from EF using $j$$HNO_3$ = 7 × 10^{-7} s^{-1}.

Table S3. Pearson correlation coefficients (R) between $j_{pNO_3^-\rightarrow HONO}$ and other factors.

Factor (Concentration)	R	Factor (Proportion in $PM_{2.5}$)	R
[NO_3^-]	-0.357	NO_3^-	-0.671
[SO_4^{2-}]	-0.095	SO_4^{2-}	-0.113
[Cl^-]	-0.037	Cl^-	0.2
[Na^+]	0.109	Na^+	0.283
[NH_4^+]	-0.300	NH_4^+	-0.562
[K^+]	-0.234	K^+	-0.253
[Mg^{2+}]	-0.113	Mg^{2+}	0.669
[Ca^{2+}]	-0.234	Ca^{2+}	0.361
[H^+]	0.629		

Table S4. Summary of the $j_{pNO_3^-}$ applied in different modeling studies.

Location	Date	$j_{pNO_3^-}$ (s^{-1})	Sources	Reference
Beijing, China	Dec 7–22, 2015	2.1×10^{-5}	Max value, field combined with model[9]	10
Wangdu, China	Dec 3–24, 2017	2.1×10^{-5}		11
Fort Worth, Texas, US	May 30–Jul 1, 2011	2.2×10^{-5}	Mean value, Pyrex surface, chamber[12]	13
Pasadena, CA, US	May–Jun, 2010	3.4×10^{-5}	Median value, various surface,	15

			chamber[14]	
Pearl River Delta, China	Jan 4–8, 2017	8.3×10^{-5}	Median value, ambient particle,	16
Changzhou, China	Apr 3–24, 2017	8.3×10^{-5}	chamber[4]	17
Beijing, China	May 7–30, 2017 Jan 15–30, 2018	8.3×10^{-5}		18
Beijing, China	Apr 24–May 4, 2018	8.3×10^{-5}		19
Beijing, China	May 25–Jul 15, 2018 Nov 26, 2018–15 Jan, 2019	8.3×10^{-5}		20
Wangdu, China	Jun 8–Jul 5, 2014	1.3×10^{-4}	Mean value, ambient particle,	21
Beijing, China	Aug 23–Sep 17, 2018	1.3×10^{-4}	chamber[4]	22
Southeastern US	Jun–Jul, 2013	2×10^{-4}	Median value, field observations[7]	23

Supplementary Figures

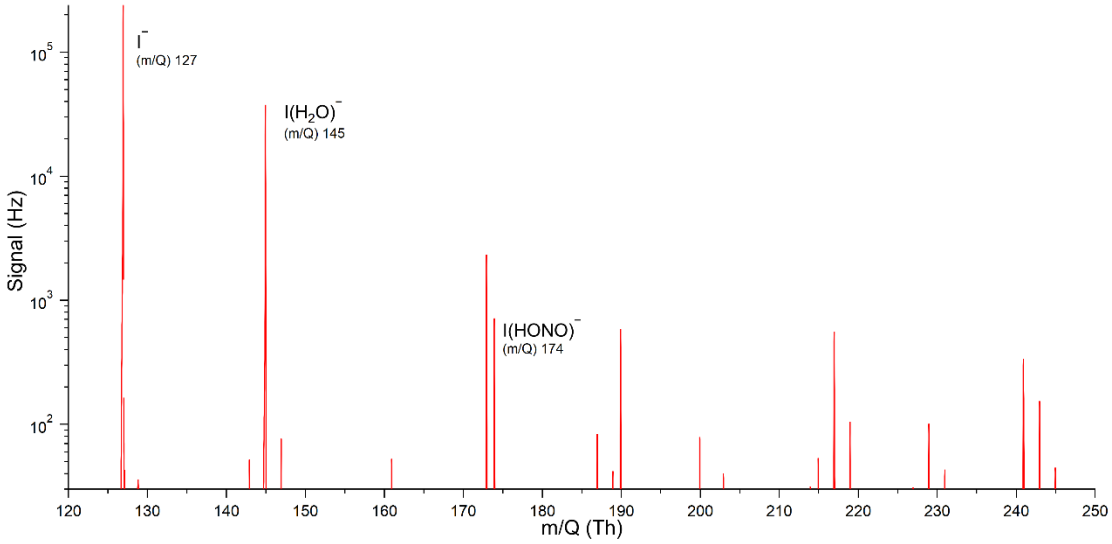

Figure S1. An example of CIMS average spectra taken from a filter sample (Dezhou 2019.01.02).

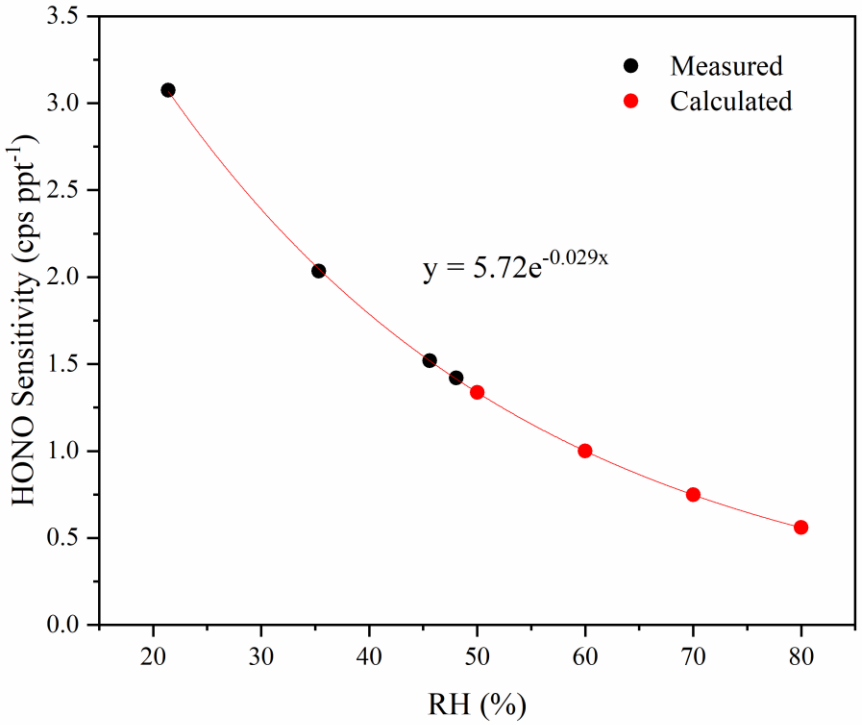

Figure S2. The sensitivity of HONO measurements by ToF-CIMS as a function of RH. Black dots are the sensitivities directly measured. Red dots are the calculated sensitivities by the fitted equation.

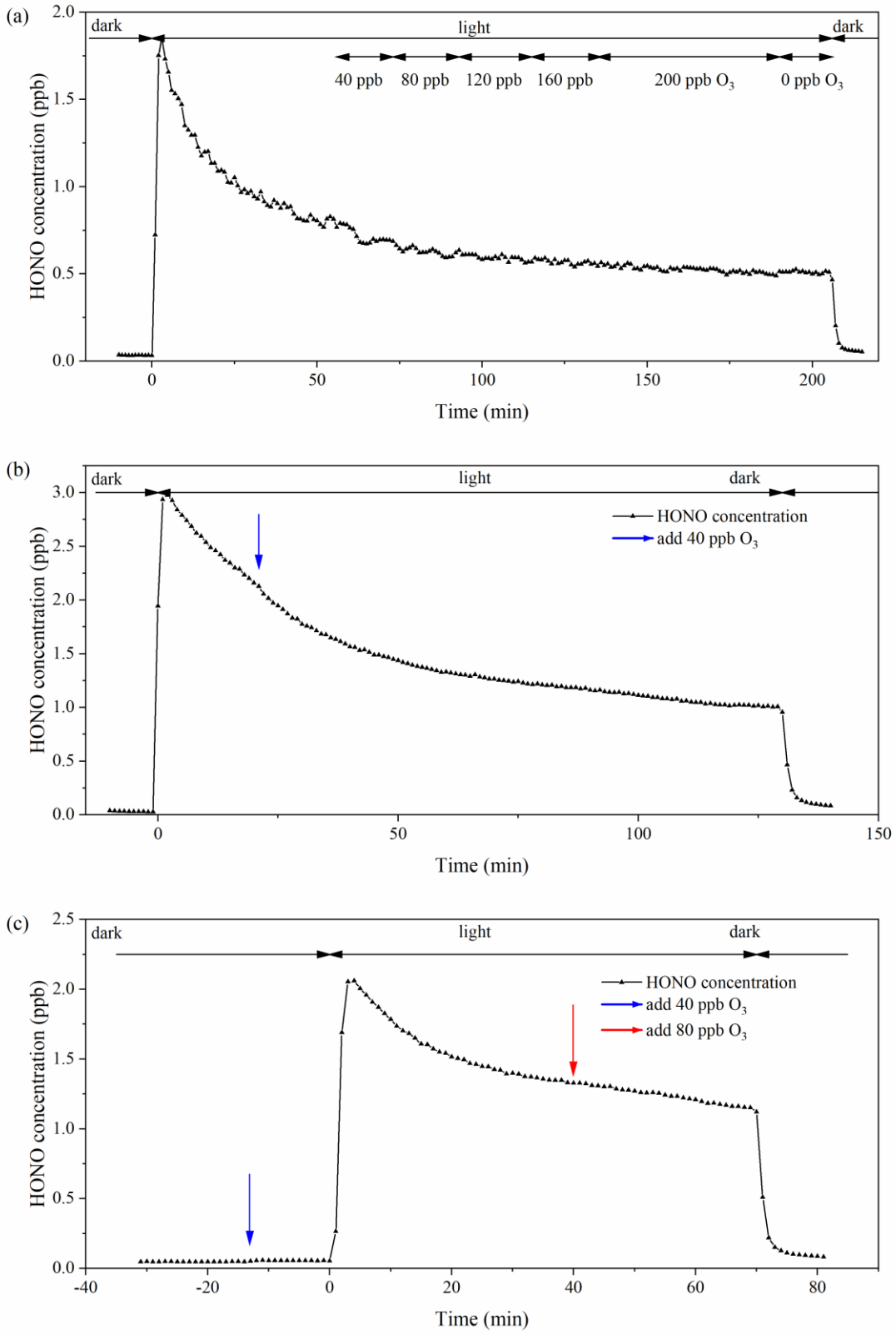

Figure S3. The time series of HONO concentrations under various experimental conditions to assess the effect of ozone (O_3). The experiments included: (a) incrementally adding O_3 at 40 ppb intervals from 0 to 200 ppb, (b) introducing 40 ppb

O_3 20 minutes after turning on the light, and (c) introducing 40 ppb O_3 before turning on the light.

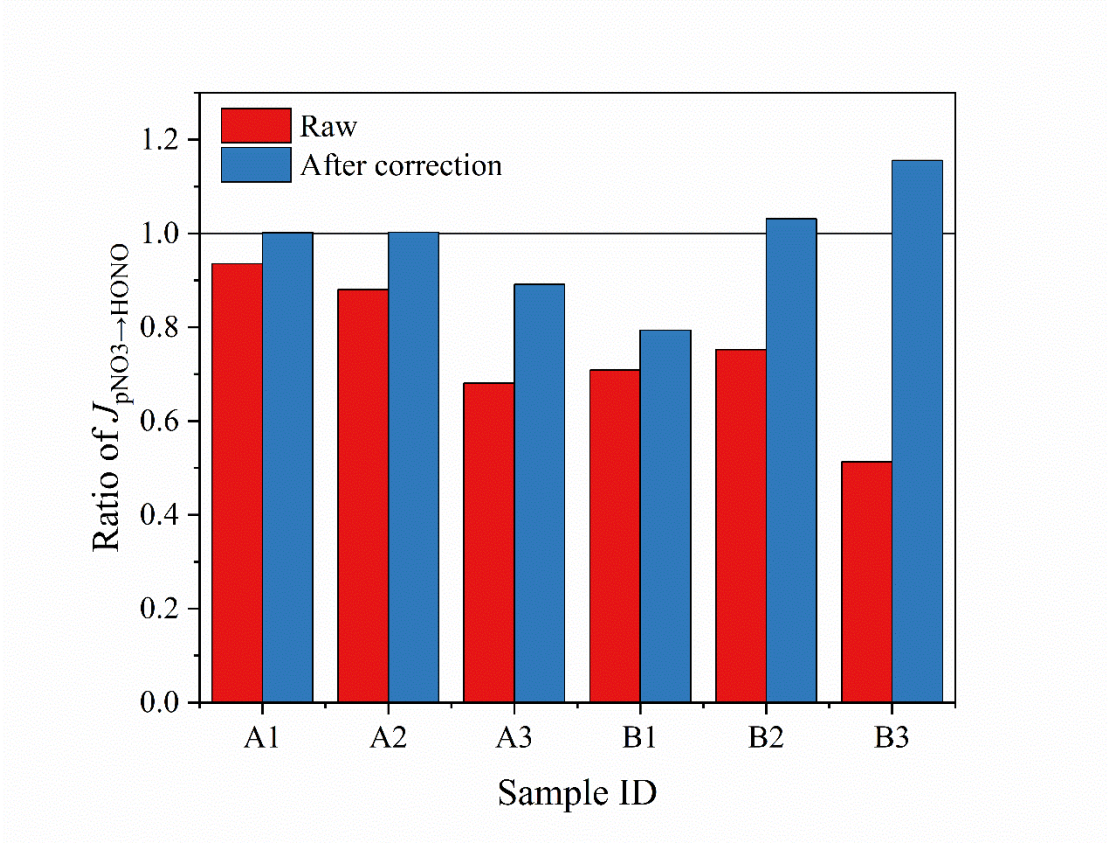

Figure S4. The comparison between the raw and corrected ratios of $j_{pNO_3^-\rightarrow HONO}$ under conditions of high and low aerosol loadings in each pair of parallel shadow effect experiments. The black horizontal line denotes a ratio value of 1. A1 refers to the comparative experiment involving AL1 and AH1, with A2 and others following the same nomenclature.

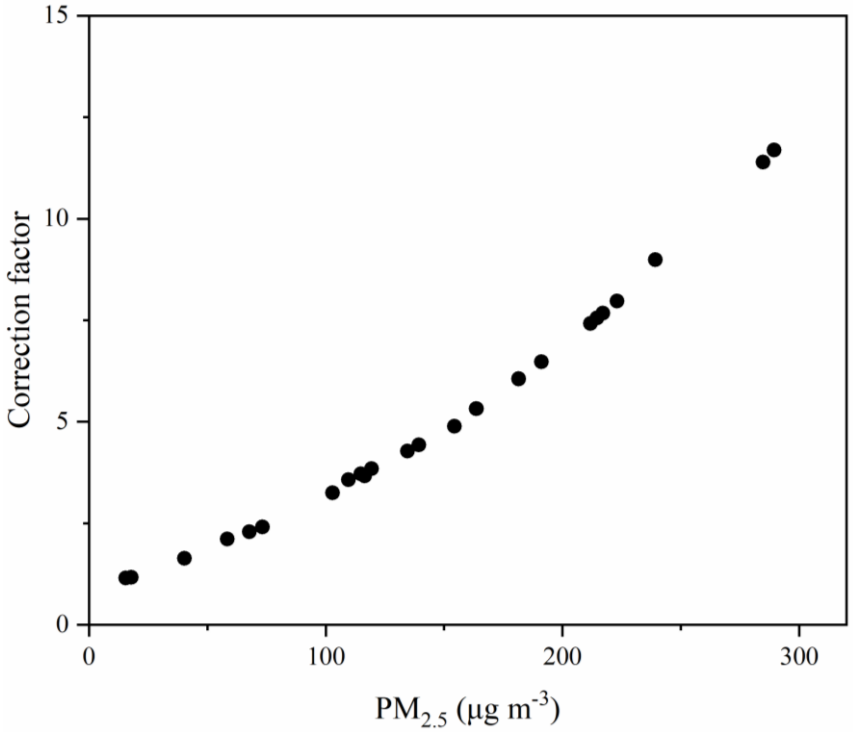

Figure S5. The correction factor of $j_{\mathrm{pNO_3^-}\rightarrow\mathrm{HONO}}$ as a function of ambient $PM_{2.5}$ concentration. The correction factor was calculated by dividing the corrected $j_{\mathrm{pNO_3^-}\rightarrow\mathrm{HONO}}$ value by the original value.

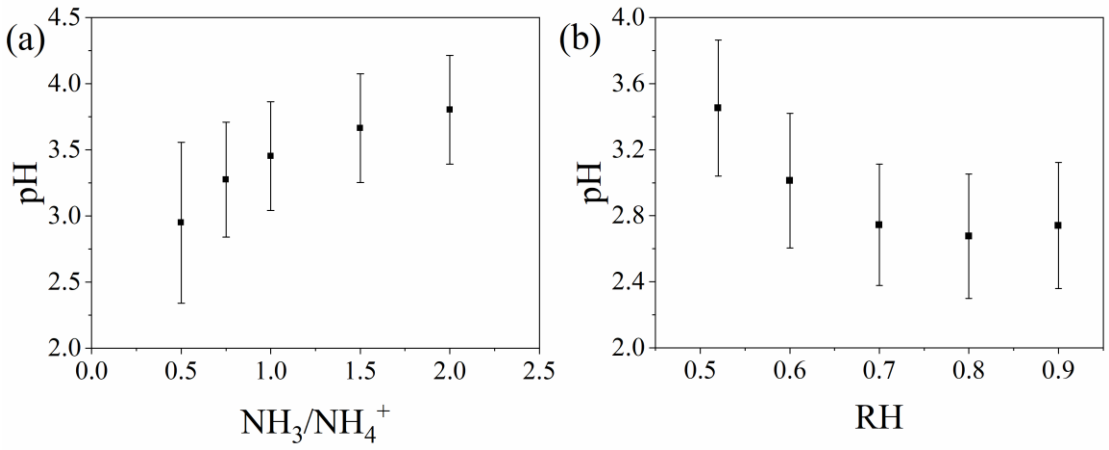

Figure S6. The E-AIM sensitivity tests of average pH on (a) NH_3 input and (b) RH input.

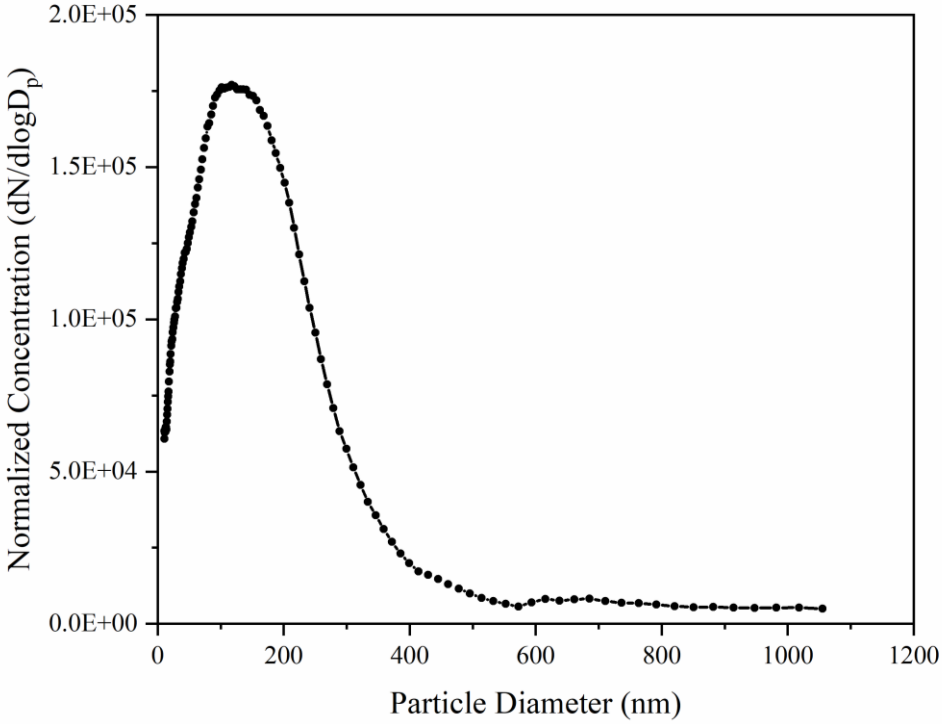

Figure S7. The normalized particle size distribution of Qingdao samples. dN denotes particle number concentrations in individual channels; $dlogD_p$ means the difference in the logarithm of the channel width.

References

1. Chu, L.; Anastasio, C. Quantum Yields of Hydroxyl Radical and Nitrogen Dioxide from the Photolysis of Nitrate on Ice. J. Phys. Chem. A 2003, 107 (45), 9594–9602. https://doi.org/10.1021/jp0349132.
2. Wexler, A. S.; Clegg, S. L. Atmospheric Aerosol Models for Systems Including the Ions H^+, NH_4^+, Na^+, SO_4^{2-}, NO_3^-, Cl^-, Br^-, and H_2O. J. Geophys. Res.: Atmos. 2002, 107 (D14), ACH 14-1-ACH 14-14. https://doi.org/10.1029/2001JD000451.
3. Meng, Z.; Xu, X.; Lin, W.; Ge, B.; Xie, Y.; Song, B.; Jia, S.; Zhang, R.; Peng, W.; Wang, Y.; Cheng, H.; Yang, W.; Zhao, H. Role of Ambient Ammonia in Particulate Ammonium Formation at a Rural Site in the North China Plain. Atmos. Chem. Phys. 2018, 18 (1), 167–184. https://doi.org/10.5194/acp-18-167-2018.
4. Ye, C.; Zhang, N.; Gao, H.; Zhou, X. Photolysis of Particulate Nitrate as a Source of HONO and NO_x. Environ. Sci. Technol. 2017, 51 (12), 6849–6856. https://doi.org/10.1021/acs.est.7b00387.
5. Bao, F.; Li, M.; Zhang, Y.; Chen, C.; Zhao, J. Photochemical Aging of Beijing Urban $PM_{2.5}$: HONO Production. Environ. Sci. Technol. 2018, 52 (11), 6309–

6316. https://doi.org/10.1021/acs.est.8b00538.
6. Zhu, Y.; Wang, Y.; Zhou, X.; Elshorbany, Y. F.; Ye, C.; Hayden, M.; Peters, A. J. An Investigation into the Chemistry of HONO in the Marine Boundary Layer at Tudor Hill Marine Atmospheric Observatory in Bermuda. Atmos. Chem. Phys. 2022, 22 (9), 6327–6346. https://doi.org/10.5194/acp-22-6327-2022.
7. Ye, C.; Zhou, X.; Pu, D.; Stutz, J.; Festa, J.; Spolaor, M.; Tsai, C.; Cantrell, C.; Mauldin, R. L.; Campos, T.; Weinheimer, A.; Hornbrook, R. S.; Apel, E. C.; Guenther, A.; Kaser, L.; Yuan, B.; Karl, T.; Haggerty, J.; Hall, S.; Ullmann, K.; Smith, J. N.; Ortega, J.; Knote, C. Rapid Cycling of Reactive Nitrogen in the Marine Boundary Layer. Nature 2016, 532, 489–491. https://doi.org/10.1038/nature17195.
8. Shi, Q.; Tao, Y.; Krechmer, J. E.; Heald, C. L.; Murphy, J. G.; Kroll, J. H.; Ye, Q. Laboratory Investigation of Renoxification from the Photolysis of Inorganic Particulate Nitrate. Environ. Sci. Technol. 2021, 55 (2), 854–861. https://doi.org/10.1021/acs.est.0c06049.
9. Romer, P. S.; Wooldridge, P. J.; Crounse, J. D.; Kim, M. J.; Wennberg, P. O.; Dibb, J. E.; Scheuer, E.; Blake, D. R.; Meinardi, S.; Brosius, A. L.; Thames, A. B.; Miller, D. O.; Brune, W. H.; Hall, S. R.; Ryerson, T. B.; Cohen, R. C. Constraints on Aerosol Nitrate Photolysis as a Potential Source of HONO and NO_x. Environ. Sci. Technol. 2018, 52 (23), 13738–13746. https://doi.org/10.1021/acs.est.8b03861.
10. Zhang, S.; Sarwar, G.; Xing, J.; Chu, B.; Xue, C.; Sarav, A.; Ding, D.; Zheng, H.; Mu, Y.; Duan, F.; Ma, T.; He, H. Improving the Representation of HONO Chemistry in CMAQ and Examining Its Impact on Haze over China. Atmos. Chem. Phys. 2021, 21 (20), 15809–15826. https://doi.org/10.5194/acp-21-15809-2021.
11. Xue, C.; Zhang, C.; Ye, C.; Liu, P.; Catoire, V.; Krysztofiak, G.; Chen, H.; Ren, Y.; Zhao, X.; Wang, J.; Zhang, F.; Zhang, C.; Zhang, J.; An, J.; Wang, T.; Chen, J.; Kleffmann, J.; Mellouki, A.; Mu, Y. HONO Budget and Its Role in Nitrate Formation in the Rural North China Plain. Environ. Sci. Technol. 2020, 54 (18), 11048–11057. https://doi.org/10.1021/acs.est.0c01832.
12. Zhou, X.; Gao, H.; He, Y.; Huang, G.; Bertman, S. B.; Civerolo, K.; Schwab, J. Nitric Acid Photolysis on Surfaces in Low-NO_x Environments: Significant Atmospheric Implications. Geophys. Res. Lett. 2003, 30 (23), 10–13. https://doi.org/10.1029/2003GL018620.
13. Gall, E. T.; Griffin, R. J.; Steiner, A. L.; Dibb, J.; Scheuer, E.; Gong, L.; Rutter, A. P.; Cevik, B. K.; Kim, S.; Lefer, B.; Flynn, J. Evaluation of Nitrous Acid Sources and Sinks in Urban Outflow. Atmos. Environ. 2016, 127, 272–282.

https://doi.org/10.1016/j.atmosenv.2015.12.044.
14. Ye, C.; Gao, H.; Zhang, N.; Zhou, X. Photolysis of Nitric Acid and Nitrate on Natural and Artificial Surfaces. Environ. Sci. Technol. 2016, 50 (7), 3530–3536. https://doi.org/10.1021/acs.est.5b05032.
15. Tuite, K.; Thomas, J. L.; Veres, P. R.; Roberts, J. M.; Stevens, P. S.; Griffith, S. M.; Dusanter, S.; Flynn, J. H.; Ahmed, S.; Emmons, L.; Kim, S. W.; Washenfelder, R.; Young, C.; Tsai, C.; Pikelnaya, O.; Stutz, J. Quantifying Nitrous Acid Formation Mechanisms Using Measured Vertical Profiles During the CalNex 2010 Campaign and 1D Column Modeling. J. Geophys. Res.: Atmos. 2021, 126 (13), e2021JD034689. https://doi.org/10.1029/2021JD034689.
16. Fu, X.; Wang, T.; Zhang, L.; Li, Q.; Wang, Z.; Xia, M.; Yun, H.; Wang, W.; Yu, C.; Yue, D.; Zhou, Y.; Zheng, J.; Han, R. The Significant Contribution of HONO to Secondary Pollutants during a Severe Winter Pollution Event in Southern China. Atmos. Chem. Phys. 2019, 19 (1), 1–14. https://doi.org/10.5194/acp-19-1-2019.
17. Shi, X.; Ge, Y.; Zheng, J.; Ma, Y.; Ren, X.; Zhang, Y. Budget of Nitrous Acid and Its Impacts on Atmospheric Oxidative Capacity at an Urban Site in the Central Yangtze River Delta Region of China. Atmos. Environ. 2020, 238, 117725. https://doi.org/10.1016/j.atmosenv.2020.117725.
18. Gu, R.; Shen, H.; Xue, L.; Wang, T.; Gao, J.; Li, H.; Liang, Y.; Xia, M.; Yu, C.; Liu, Y.; Wang, W. Investigating the Sources of Atmospheric Nitrous Acid (HONO) in the Megacity of Beijing, China. Sci. Total Environ. 2022, 812, 152270. https://doi.org/10.1016/j.scitotenv.2021.152270.
19. Zhang, W.; Tong, S.; Jia, C.; Wang, L.; Liu, B.; Tang, G.; Ji, D.; Hu, B.; Liu, Z.; Li, W.; Wang, Z.; Liu, Y.; Wang, Y.; Ge, M. Different HONO Sources for Three Layers at the Urban Area of Beijing. Environ. Sci. Technol. 2020, 54 (20), 12870–12880. https://doi.org/10.1021/acs.est.0c02146.
20. Liu, J.; Liu, Z.; Ma, Z.; Yang, S.; Yao, D.; Zhao, S.; Hu, B.; Tang, G.; Sun, J.; Cheng, M.; Xu, Z.; Wang, Y. Detailed Budget Analysis of HONO in Beijing, China: Implication on Atmosphere Oxidation Capacity in Polluted Megacity. Atmos. Environ. 2021, 244, 117957. https://doi.org/10.1016/j.atmosenv.2020.117957.
21. Liu, Y.; Lu, K.; Li, X.; Dong, H.; Tan, Z.; Wang, H.; Zou, Q.; Wu, Y.; Zeng, L.; Hu, M.; Min, K. E.; Kecorius, S.; Wiedensohler, A.; Zhang, Y. A Comprehensive Model Test of the HONO Sources Constrained to Field Measurements at Rural North China Plain. Environ. Sci. Technol. 2019, 53 (7), 3517–3525. https://doi.org/10.1021/acs.est.8b06367.
22. Jia, C.; Tong, S.; Zhang, W.; Zhang, X.; Li, W.; Wang, Z.; Wang, L.; Liu, Z.; Hu,

B.; Zhao, P.; Ge, M. Pollution Characteristics and Potential Sources of Nitrous Acid (HONO) in Early Autumn 2018 of Beijing. Sci. Total Environ. 2020, 735, 139317. https://doi.org/10.1016/j.scitotenv.2020.139317.

23. Ye, C.; Zhou, X.; Pu, D.; Stutz, J.; Festa, J.; Spolaor, M.; Tsai, C.; Cantrell, C.; Mauldin, R. L.; Weinheimer, A.; Hornbrook, R. S.; Apel, E. C.; Guenther, A.; Kaser, L.; Yuan, B.; Karl, T.; Haggerty, J.; Hall, S.; Ullmann, K.; Smith, J.; Ortega, J. Tropospheric HONO Distribution and Chemistry in the Southeastern US. Atmos. Chem. Phys. 2018, 18 (12), 9107–9120. https://doi.org/10.5194/acp-18-9107-2018.